EVAPORATION OF LIQUID DROPLETS ON FLAT AND CURVED SOLID SUBSTRATES

Amirhossein Amini

A dissertation
submitted in partial fulfillment of the
requirements for the degree of

Doctor of Philosophy

University of Washington

2017

Reading Committee:

George M. Homsy & James J. Riley, Chair

Albeto Aliseda

Program Authorized to Offer Degree:
Mechanical Engineering

University of Washington

Abstract

EVAPORATION OF LIQUID DROPLETS ON FLAT AND CURVED SOLID SUBSTRATES

Amirhossein Amini

Chair of the Supervisory Committee:
Chair George M. Homsy & James J. Riley
Mechanical Engineering

We study the evaporation of liquid droplets on flat and curved heated substrates. We derive an evolution equation for the drop thickness to evaluate its shape as it evaporates on a curved substrate. We adopt a one-sided model with thermal control which, together with the lubrication approximation, results in an evolution equation for the local height of the droplet. Without requiring any pre-assumption for the shape of the drop, we formulate the problem for the two modes of evaporation: (i) pinned contact line and (ii) moving contact line with fixed contact angle. For each evaporation mode, we solve the problem numerically for flat and curved solid substrates, separately.

We first analyze the simplified evolution equation for the case of flat solid substrates. For the pinned contact line case, we observe that after a time interval the contact angle, i.e. the angle between the solid and the interface at the contact line, dynamics become nonlinear and, interestingly, the local contact angle goes to zero in advance of total evaporation of the drop. For the case of moving contact line, in which the singularity at the contact line is treated by a numerical slip model, we find that the droplet nearly keeps its initial circular shape and that the contact line recedes with constant speed.

We then analyze the problem for various periodic and quasi-periodic substrate profiles. For the case of pinned contact line, we find the results to be very similar to the flat case. For

the case of moving contact line, we study the dynamics of the contact line and the apparent contact angle, i.e. the angle that the liquid appears to make with the solid surface when viewed at such a coarse resolution that the substrate appears flat (the angle between the horizon and the interface at the contact line). In contrast with our results for a flat substrate, for which the contact line recedes at a nearly constant speed, we observe that the contact line speed and position show significant time variation and that the contact line moves in an approximately step-like fashion on relatively steep substrates. For the simplest case of a periodic substrate, we find that the apparent contact angle is periodic in time. For doubly periodic substrates, we find that the apparent contact angle is again periodic and that the problem exhibits a phase-locking behavior. For multi-mode quasi-periodic substrates, we find the contact line behavior to be temporally complex and not only limited to an approximately step-like motion. In all cases, we find that the overall evaporation is increased relative to the flat substrate.

TABLE OF CONTENTS

LIST OF FIGURES

Chapter 1

INTRODUCTION

In this work we study the evaporation of a liquid droplet on both flat and curved solid substrates. Our work was originally motivated by the work of McHale *et al.* [14] in which they consider the evaporation process of a small water droplet from structured polymer surfaces. As illustrated in their Figure 2, they observe all three modes of evaporation: initially the droplet evaporates in the pinned contact line mode; once a critical contact angle is approached, the contact line depins and, in contrast with what occurs on a smooth surface, the contact line moves in a step-like fashion while the contact angle remains approximately constant; finally, in the last and relatively shortest stage of the evaporation, both the wetted radius and the contact angle decrease simultaneously until the entire droplet is evaporated. As far as we are aware, virtually all the work done on modeling evaporation of droplets is for mathematically smooth surfaces. We review some of that work below. Consequently, we decided to analyze the evaporation of droplets places on surfaces with topography.

Evaporation of sessile droplets are particularly interesting due to the complexity associated with modeling the evaporative mass flux, different modes of evaporation, and the large stresses that build up near moving contact lines. A heated droplet evaporates because of an imbalance between the vapor pressure and the pressure in the gas. The rate of evaporation is determined by a combination of the rate at which energy diffuses through the liquid, resulting in a rise in the surface temperature, and the rate at which molecules that have been transported from the liquid to the vapor can diffuse away. Thus, to fully treat the evaporative flux an excessively complex two-sided model is required in which both effects are considered. As fully explained by Murisic & Kondic [17] the two sided model can be

simplified by assuming that the vapor is convection-free and that the vapor viscosity and thermal conductivity are much smaller than their liquid counterparts. Models at this stage are still rather complex. To simplify, one may choose to focus on the vapor concentration which results into diffusion-limited models (see, for example, Popov [22] and Cazabat [4]) or on the liquid phase, which yields a thermal control one-sided model (see Burelbach *et al.* [3]). However, these two models differ only slightly in their predictions regarding main features of the evaporative flux and what one learns in one case is generally applicable to the other. In this work, identical to the method used by Ajaev & Homsy [1], the one-sided thermal model is utilized to relate the evaporative mass flux to thermodynamic properties of the liquid-vapor interface.

Previous observations [22] show that during the beginning phases of evaporation the contact line remains pinned while the contact angle decreases. When a critical angle is reached, the contact line begins to move. As far as we know, the only model that predicts this critical angle is that of Stauber et al. In their very recent work [24], they propose that for contact angles larger than a critical angle, referred to as θ^*, the contact line is pinned by a tangential force. They compute a critical force using Young's equation and the assumptions that θ^* is the angle at which this critical tangential force is reached and that the value of such force is independent of both initial contact angle and θ^*. As a result, they provide an explicit condition that determines θ^* as a function of the critical force and the initial contact angle. The moving phase initially occurs in a constant contact angle mode followed by a second moving phase in which both the contact angle and contact radius vary. Although as the contact line moves the contact angle may or may not change, many authors including Picknett & Bexon [18] and Wilson *et al.* [23] report that in practice the second moving phase is often relatively short compared with the other two modes. In this work, the evaporation of droplet is considered separately for the two extreme modes: pinned contact line and moving contact line with constant contact angle. We leave the issue of transition from pinned to moving mode for future work.

Problems involving moving contact lines are intrinsically associated with a singularity at the

contact line. The fluid velocity is finite on the liquid-vapor interface and set to be zero by the no-slip condition on the solid surface. This results into a nonphysical shear stress singularity indicating that an infinite force is required to move the contact line (see for example Dussan V. *et al.* [8]). As Mazouchi *et al.* [13] nicely cover in the introduction to their paper, three main models are developed to eliminate the contact line singularity: precursor film, slip, and numerical slip models. Supported by experimental observations, the precursor model (Dussan V. *et al.* [5] and Kondic & Bertozzi [12]) assumes that instead of the true contact between vapor, liquid and solid, the dry solid ahead of the contact line is covered with a very thin film, i.e. the precursor film. The slip model (Dussan V. *et al.* [7] and Greenspan [10]), which allows the three phases to contact at an actual point, relaxes the no-slip condition in a distance, referred to as the slip length, near the contact line and employs the no-slip condition outside. This model uses a Navier slip type condition associated with a slip coefficient. Haley & Miksis [11] numerically compare different types of these slip coefficients and show that the qualitative features of the contact line motion are similar in all cases. The numerical slip model (Moriarty & Shwartz [15]) treats the contact line singularity at the stage of numerically solving the problem. This model employs finite difference schemes to model the motion of contact line with a contact angle boundary condition prescribed. The problem is discretized, avoiding putting a node or a mesh point directly at the contact line. The position of the contact line is then allowed to vary (slip) until a prescribed contact angle is met. Moriarty & Shwartz [15] showed that numerical slip and a Navier slip model give very similar results as long as the slip length and the numerical grid spacing are similar in magnitude. In this work, the numerical slip model is utilized to model the contact line motion while the contact angle is fixed to be constant.

There have been a wide range of theoretical studies related to the evaporation of liquid droplets on flat solid substrates, both in pinned and moving contact line modes. These models either assume the droplet keeps its initial static shape as it evaporates (e.g. [6]) or use a global mass balance as a boundary condition to solve the evolution equation (e.g. [2]). The former type of model analyzes the problem using only a mass balance, once the evaporative

flux is modeled. Although assuming that the droplet shape remains circular is approximately valid for evaporation on flat substrates, and such models are able to produce results that are in agreement with experimental data, we believe that this assumption should not be initially imposed but rather be confirmed by the solution of a well-posed moving boundary problem. Moreover, such an assumption fails when the solid substrate is not flat. Particularly, for the case of evaporation with moving contact line and fixed contact angle on a non-flat solid, which we address in this work, the droplet profiles vary from the initial circular shape. The latter type of model, which does not assume a circular shape over the entire process, considers the governing equations within the bulk liquid and on the interface and typically uses lubrication theory to produce a single evolution equation. When solving the evolution equation it employs a global mass balance as a boundary condition. We believe that the global mass balance has been already applied to the problem at the stage of deriving the evolution equation via conservation of mass and interfacial mass balance and hence it should not be reused as a boundary condition. Therefore, we found it to be necessary to develop a model that neither assumes a circular cross-section over the entire process and nor employs the global mass balance as a boundary condition. Such a model can be expanded easily to non-flat substrates and is able to analyze both evaporation modes in a similar manner. Accordingly, we formulate the problem based on a boundary condition of no capillary flow into the contact line.

As far as we are aware, the problem of evaporating droplets on curved substrates is yet to be analyzed and additional research is required to understand the dynamics of the contact line as the droplet evaporates on a non-planar solid substrate. However, recent work has considered the dynamic contact line motion over a variety of non-planar substrates driven by either capillary pressure or gravity. Savva and Kalliadasis [19] consider the spreading on horizontal non-planar substrates of a two-dimensional droplet that has an initial shape different than the equilibrium profile. They consider different single-mode sinusoidal substrates, a trench, and a ridge, with the single mode sinusoid being most relevant to our work here. In similar work, Savva and Kalliadasis [20] consider gravity driven motion of a drop on an inclined rough

surface. The results in both of these papers demonstrate that in the case of a sinusoidal single mode substrate, the contact line exhibits an apparent "stick-slip" behavior wherein it spends considerable time moving very slowly, giving the appearance of being pinned. Savva *et al.* [21] generalized these observations by considering spreading over a random rough surface that is constructed from periodic waveforms with random Fourier coefficients. They find that the contact line response is also random, and that spreading is inhibited by roughness. Espin and Kumar [9] provided a model of a spreading droplet on a single curved "bump" and commented on the potential for structured surfaces to produce "apparent stick-slip" behavior. By adopting the word "apparent", they emphasize that the pinning stage during the stick-slip motion needs to be interpreted as an apparent pinning since the contact line may still move very slowly. Here, we will use the "apparent stick-slip" or "apparent step-like" terminology for the same reason described by these authors: the contact line may still move very slowly during the apparent "pinning" stage.

In this work, we derive an evolution equation for the drop thickness to evaluate its shape as it evaporates on a curved substrate. The appropriate contact line conditions are provided separately for the two modes of evaporation. A numerical algorithm is developed to solve the evolution equation in time. Flat and periodic solid surfaces are considered and for each case the solution of the evolution equation is presented for both evaporation modes. The droplet shape, evaporative mass flux and contact angle are presented for the case in which the contact line is pinned. The droplet shape, evaporative mass flux, wetted radius, contact line speed and apparent contact angle are shown for the case of moving contact line. For the case of moving contact line on periodic substrates, we consider a single-mode harmonic solid as the simplest case; we study the dynamics of the contact line and the apparent contact angle and show that an apparent stick-slip motion is captured by our model. We compare these results to the flat case and establish the characteristics of the contact line motion. We then create more complex substrate profiles by adding more modes, including quasi-periodic wave forms, and compare the results with the simpler cases.

Chapter 2

FORMULATION FOR THE CASE OF CURVED SOLID SUBSTRATE

Consider a liquid layer, initially part of a cylinder with circular cross-section, evaporating on a curved solid substrate as shown in Figure 2.1. Suppose that the solid is rigid and impermeable, that the temperature of the solid substrate at the vicinity of the liquid is larger than the saturation temperature of the liquid, and that the liquid is incompressible and Newtonian. The purpose of the present chapter is to derive an evolution equation accompanied with appropriate boundary conditions for the height of the evaporating liquid layer under the influence of viscous forces and surface tension, for the following two modes of evaporation:

I) pinned contact line: the wetted radius remains constant and the contact angle decreases.

II) moving contact line: the contact angle remains constant and the wetted radius decreases.

The derivation is based on one-sided model and the lubrication approximation, in conjunction with the following assumptions:

- the solid-liquid interface does not vary along the axis of the liquid layer and is symmetric about the radial axis crossing the point on the liquid-vapor interface at which the liquid height is maximum.
- the flow in the liquid does not vary along the axis of the liquid layer;
- the vapor is quiescent and at constant pressure;
- the surface tension of the interface between the liquid and the vapor is constant;

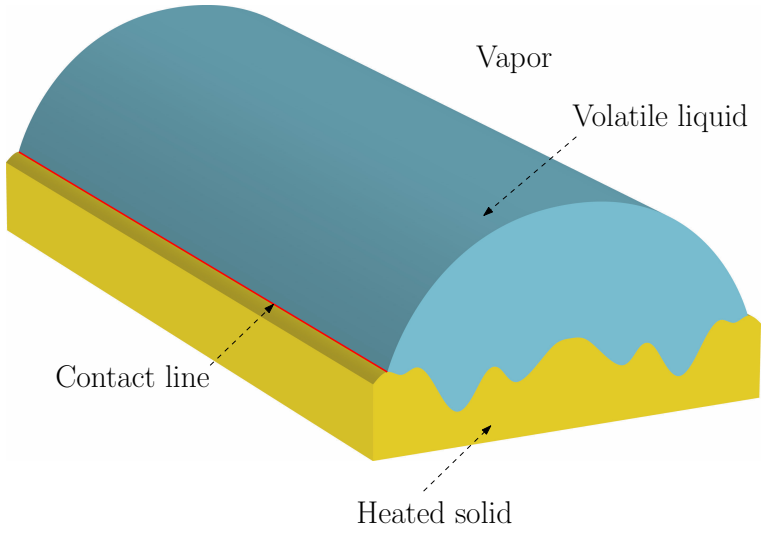

Figure 2.1: 3D view of a liquid layer evaporating on a curved solid substrate.

- the liquid droplet is thin but not so thin that van der Waals forces are significant;
- external forces, in particular gravity, are negligible.

In view of the assumptions that the solid-liquid interface does not vary along the axis of the liquid layer and is symmetric about the vertical axis, that the flow in the liquid does not vary along the axis of the liquid layer, and that the liquid layer is initially part of a cylinder with circular cross-section, the problem is analyzed in symmetric 2D space. A schematic of a generic cross-section of the liquid layer evaporating on a curved solid substrate is provided in Figure 2.2, which represents chosen conventions for the orientation of unit tangent and normal vectors $\mathbf{t}$ and $\mathbf{n}$ for the liquid-vapor interface. The temperature of the solid-liquid interface is known and denoted by T_w. The temperature of the liquid-vapor interface, which is unknown and will be determined as a result of solving the problem, is denoted by T_i. The constant surface tension acting on the liquid-vapor interface is denoted by σ, the evaporative mass flux is denoted by J, and the constant pressure of the vapor and the vapor mass density are denoted by p_v and ρ_v. The liquid mass density, shear viscosity, thermal conductivity, specific heat capacity, and specific latent heat are respectively denoted by ρ, μ, k, c, and $\mathcal{L}$ and are assumed to be constant.

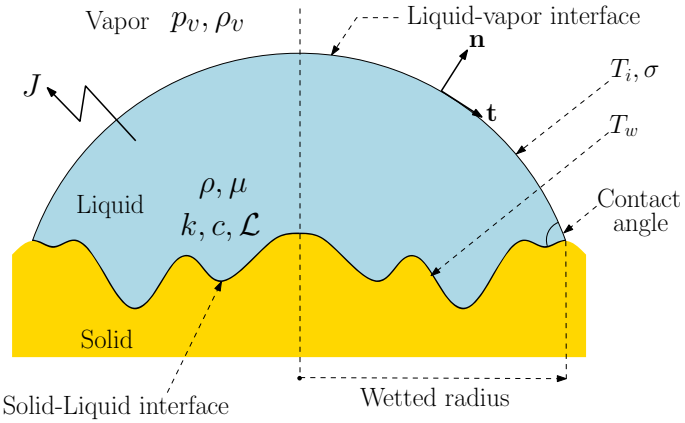

Figure 2.2: Schematic of a generic cross-section of the liquid layer evaporating on a curved solid substrate.

2.1 Governing equations and boundary conditions

The governing equations inside the liquid that are required to analyze the problem are: conservation of mass, linear momentum balance, and conservation of energy. In view of the incompressibility of the liquid, continuity requires that

$$\nabla \cdot \mathbf{v} = 0, \tag{2.1}$$

and, in view of the assumptions that external forces, in particular gravity, are negligible and the liquid is incompressible and Newtonian, the linear momentum balance indicates that

$$\rho(\mathbf{v}_t + \mathbf{v} \cdot \nabla \mathbf{v}) = -\nabla p + \mu \nabla^2 \mathbf{v}. \tag{2.2}$$

Granted that mass density, specific heat capacity and thermal conductivity of the liquid are constant the energy balance requires that

$$T_t + \mathbf{v} \cdot \nabla T = \chi \nabla^2 T, \tag{2.3}$$

where t represents time and $\mathbf{v}$, p and T are respectively, the velocity, pressure and temperature of the liquid and χ is the thermal diffusivity defined as

$$\chi = \frac{k}{\rho c} \cdot$$

The interfacial conditions that are required to be considered are: mass balance, momentum balance (normal and tangential stresses), energy balance, and thermodynamic-kinetic equation for the evaporative mass flux. The interfacial mass balance at the location of the liquid-vapor interface implies that

$$J = \rho(\mathbf{v} - \mathbf{v}^I) \cdot \mathbf{n}, \tag{2.4}$$

where $\mathbf{v}$ is the fluid velocity at liquid-vapor interface, and $\mathbf{v}^I$ is the velocity of the liquid-vapor interface. The normal component of the interfacial linear momentum balance at the liquid-vapor interface requires that

$$[\![\mathbf{n} \cdot \mathbf{T} \cdot \mathbf{n}]\!] = 2H\sigma - p_v, \tag{2.5}$$

where $2H$ is the mean curvature of the liquid-vapor interface, $\mathbf{T}$ is the liquid stress tensor at the location of the liquid-vapor interface, and $[\![\cdots]\!]$ denotes a jump across the interface from liquid to vapor. Granted that the surface tension is constant, the tangential component of the interfacial linear momentum balance at liquid-vapor interface requires that

$$[\![\mathbf{t} \cdot \mathbf{T} \cdot \mathbf{n}]\!] = 0. \tag{2.6}$$

The interfacial energy balance at the liquid-vapor interface indicates that

$$J\mathcal{L} = -k\nabla T \cdot \mathbf{n}. \tag{2.7}$$

To relate the evaporative mass flux J to the thermodynamic properties of the liquid-vapor interface, a thermodynamic-kinetic equation is developed based on the classical Hertz-Knudsen formula [1] accompanied with linearized Clausius-Clapeyron equation, which requires that

$$J = \rho_v \sqrt{\frac{R_M T_i}{2\pi}} \left[\frac{p - p_v}{\rho R_M T_s} + \frac{\mathcal{L}}{R_M T_s} (\frac{T_i}{T_s} - 1) \right], \tag{2.8}$$

where p is the liquid pressure at the liquid-vapor interface, T_s is the liquid saturation temperature and R_M is the universal gas coefficient per unit mass.

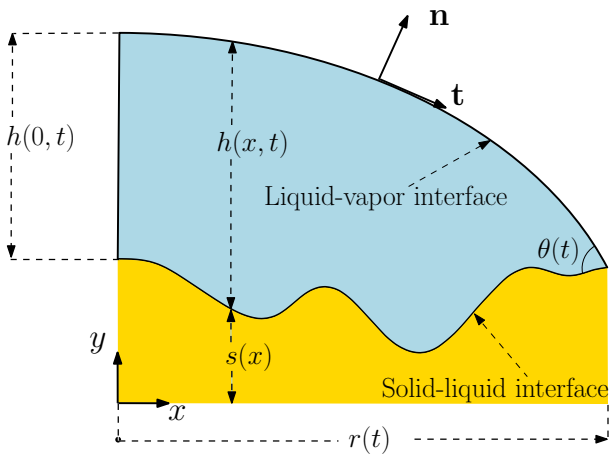

Figure 2.3: 2D Schematic of a symmetric liquid droplet analyzed in a Cartesian coordinate system.

Since the solid is assumed to be rigid and impermeable, the no-slip and no-penetration conditions indicate that

$$\mathbf{v} = 0, \tag{2.9}$$

at the solid-liquid boundary. The temperature boundary condition requires that

$$T = T_w, \tag{2.10}$$

along the solid-liquid interface.

2.2 Governing equations and boundary conditions in Cartesian coordinates

Since the problem is assumed to be 2D symmetric, a Cartesian coordinate system is employed to analyze the problem. In this section, governing equations and boundary conditions provided in 2.1 are derived in the Cartesian coordinates shown in Figure 2.3, in which $x = 0$ represents the symmetry line. In Figure 2.3, $h(x, t)$ denotes the thickness of the liquid layer, $s(x)$ denotes the y-component of the solid-liquid interface position, $r(t)$ denotes the wetted radius and $\theta(t)$ denotes the contact angle. Considering that u and v are referred to as the

lateral and transverse components of fluid velocity $\mathbf{v}$, in Cartesian coordinates, continuity takes the form of

$$u_x + v_y = 0, \tag{2.11}$$

linear momentum balance in x-direction is

$$\rho(u_t + uu_x + vu_y) = -p_x + \mu(u_{xx} + u_{yy}), \tag{2.12}$$

linear momentum balance in y-direction requires that

$$\rho(v_t + uv_x + vv_y) = -p_y + \mu(v_{xx} + v_{yy}), \tag{2.13}$$

and energy balance reduces to

$$T_t + uT_x + vT_y = \chi(T_{xx} + T_{yy}). \tag{2.14}$$

The normal and tangential vectors $\mathbf{n}$ and $\mathbf{t}$ to the liquid-vapor interface, shown in Figure 2.3, take the following form in Cartesian coordinates,

$$\mathbf{n} = \Big[-(h_x + s_x), 1\Big]\Big(1 + (h_x + s_x)^2\Big)^{-1/2}, \qquad \text{and,} \qquad \mathbf{t} = \Big[1, h_x + s_x\Big]\Big(1 + (h_x + s_x)^2\Big)^{-1/2}. \tag{2.15}$$

and the stress tensor $\mathbf{T}$ is defined as

$$\mathbf{T} = \begin{bmatrix} -p + 2\mu u_x & \mu(u_y + v_x) \\ \\ \mu(u_y + v_x) & -p + 2\mu v_y \end{bmatrix}. \tag{2.16}$$

Using the above definitions for $\mathbf{n}$, $\mathbf{t}$, and $\mathbf{T}$ the interfacial mass balance (2.4), the normal (2.5) and tangential (2.6) components of the interfacial linear momentum balance, and the interfacial energy balance (2.7) at the liquid-vapor interface become

$$J = \frac{\rho(-u(h+s)_x + v - h_t)}{\sqrt{1 + (h_x + s_x)^2}}, \tag{2.17}$$

$$p_v - p + 2\mu \frac{u_x(h_x + s_x)^2 + v_y - (h+s)_x(u_y + v_x)}{1 + (h_x + s_x)^2} = \frac{\sigma(h+s)_{xx}}{(1 + (h_x + s_x)^2)^{3/2}}, \tag{2.18}$$

$$\frac{2(h+s)_x(v_y - u_x) + (u_y + v_x)(1 - (h_x + s_x)^2)}{1 + (h_x + s_x)^2} = 0, \quad \text{and} \tag{2.19}$$

$$J\mathcal{L} = -k\frac{(h+s)_x T_x + T_y}{(1 + h_x^2)^{1/2}}. \tag{2.20}$$

The thermodynamic-kinetic equation for evaporative mass flux is coordinate independent and remain the same as, i.e.

$$J = \rho_v \sqrt{\frac{R_M T_i}{2\pi}} \left[\frac{p - p_v}{\rho R_M T_s} + \frac{\mathcal{L}}{R_M T_s}(\frac{T_i}{T_s} - 1) \right]. \tag{2.21}$$

The no-slip and no-penetration conditions follow that at the solid-liquid interface

$$u = 0, \qquad \text{and,} \qquad v = 0, \tag{2.22}$$

and the temperature boundary condition at the solid-liquid interface requires that

$$T = T_w. \tag{2.23}$$

2.3 Non-dimensionalizing the governing equations and boundary conditions

Toward determining the lubrication equations, it is advantageous to first obtain dimensionless versions of the governing equations and boundary conditions. To derive the dimensionless counterparts, each variable is non-dimensionalized with reference to a specific scale. Temperature is scaled by the liquid saturation temperature T_s and its dimensionless counterpart takes the form of

$$\hat{T} = \frac{T}{T_s}. \tag{2.24}$$

Consider L_x, and, L_y as the length scales required to describe the droplet in x and y directions so that the ratio L_y/L_x characterizes the slope relevant to the liquid-vapor interface. The independent coordinate x is scaled with the droplet length scales L_x and all lengths in y-direction, including y, h, and, s, are scaled by L_y such that their dimensionless counterparts follow

$$\hat{x} = \frac{x}{L_x}, \qquad \hat{y} = \frac{y}{L_y}, \qquad \hat{h} = \frac{h}{L_y}, \qquad \text{and,} \qquad \hat{s} = \frac{s}{L_y}. \tag{2.25}$$

The initial wetted radius $r(0)$ and the initial thickness $h(0,0)$ at the symmetry location are chosen as the length scales L_x and L_y respectively. Subsequent to utilization of two different length scales to specify the droplet geometry, the continuity equation requires the introduction of two different velocity scales V_x and V_y in the x and y directions. Thus the dimensionless form of u and v are

$$\hat{u} = \frac{u}{V_x}, \qquad \text{and,} \qquad \hat{v} = \frac{v}{V_y}. \tag{2.26}$$

The interfacial energy balance (2.20) implies that the natural velocity scale for the y-component of the velocity needs to be chosen as

$$V_y = \frac{kT_s}{\rho \mathcal{L} L_y}. \tag{2.27}$$

The definition of velocity implies that the time scale T_o is defined as $T_o = L_y/V_y$ and therefore, dimensionless time $\hat{t}$ follows as

$$\hat{t} = \frac{t}{L_y/V_y}. \tag{2.28}$$

The conservation of mass (2.11) in the liquid indicates that the velocity scale V_x chosen for the x-component of the velocity is related to that in the y-direction as

$$V_x = \frac{L_x}{L_y} V_y. \tag{2.29}$$

Balancing the pressure p with σh_{xx} results into the appropriate pressure scale,

$$P_o = \frac{\sigma}{L_x^2/L_y}, \tag{2.30}$$

such that the dimensionless pressure $\hat{p}$ is defined as

$$\hat{p} = \frac{p}{\sigma L_y/L_x^2}. \tag{2.31}$$

The interfacial mass balance (2.17) requires that the evaporative mass flux J needs to be scaled by ρV_y, therefore, its dimensionless counterpart is defined as

$$\hat{J} = \frac{J}{\rho V_y}. \tag{2.32}$$

After choosing all the appropriate scales, it is advantageous to first introduce the dimensionless numbers governing the problem. The ratio of the temperature T_w of the solid-liquid interface to the saturation temperature T_s yield to a dimensionless number defined as

$$\hat{T}_w = \frac{T_w}{T_s}. \tag{2.33}$$

The ratio of droplet length scales results into a dimensionless number,

$$\epsilon = \frac{L_y}{L_x}. \tag{2.34}$$

The process of scaling x-component (2.12) of the linear momentum balance in the liquid introduces two dimensionless numbers, the Reynolds and the Capillary numbers defined as

$$\mathrm{Re} = \rho\frac{V_y L_x}{\mu}, \qquad \text{and,} \qquad \mathrm{Ca} = \frac{\mu V_y}{\sigma}. \tag{2.35}$$

Nondimensionalizing the energy balance (2.14) in the liquid introduces a dimensionless number Péclet defined as,

$$\mathrm{Pé} = \frac{V_y L_x}{\chi}. \tag{2.36}$$

During the process of nondimensionalizing the thermodynamic-kinetic equation (2.21) for the evaporative mass flux two, dimensionless numbers are introduced which are defined as,

$$M = \frac{\rho V_y \sqrt{2\pi R_M T_s}}{\rho_v \mathcal{L}}, \qquad \text{and,} \qquad N = \frac{\sigma}{\rho \mathcal{L} L_y}. \tag{2.37}$$

Finally the initial contact angle $\theta(0)$ shown in Figure 2.3 is a dimensionless number the governing the problem. To summarize, the evaporation of the droplet on a curved solid substrate is governed by no fewer than 8 dimensionless numbers,

$$\left.\begin{aligned} \hat{T}_w = \frac{T_w}{T_s}, \qquad \epsilon = \frac{L_y}{L_x}, \qquad \mathrm{Re} = \rho\frac{V_y L_x}{\mu}, \qquad \mathrm{Ca} = \frac{\mu V_y}{\sigma}, \qquad \mathrm{Pé} = \frac{V_y L_x}{\chi}, \\ M = \frac{\rho V_y \sqrt{2\pi R_M T_s}}{\rho_v \mathcal{L}}, \qquad N = \frac{\sigma}{\rho \mathcal{L} L_y}, \qquad \text{and,} \qquad \theta(0). \end{aligned}\right\} \tag{2.38}$$

With the forgoing choices of scales and considering the dimensionless numbers, governing equations and boundary conditions (2.11)-(2.23) are transformed into their dimensionless

counterparts. For the sake of simplifying the notation, the carat is dropped from all variables. The continuity equation (2.11), x-component (2.12) and y-component (2.13) of linear momentum balance and conservation of energy (2.14) inside the liquid yield their dimensionless forms,

$$u_x + v_y = 0, \tag{2.39}$$

$$\epsilon \mathrm{Re}\big(u_t + uu_x + vu_y\big) = -Ca^{-1}\epsilon^4 p_x + \epsilon^2 u_{xx} + u_{yy}, \tag{2.40}$$

$$\epsilon^3 \mathrm{Re}\big(v_t + uv_x + vv_y\big) = -Ca^{-1}\epsilon^4 p_y + \epsilon^4 v_{xx} + \epsilon^2 v_{yy}, \tag{2.41}$$

and,

$$\epsilon \mathrm{P\acute{e}}\big(T_t + uT_x + vT_y\big) = \epsilon^2 T_{xx} + T_{yy}. \tag{2.42}$$

The interfacial mass balance (2.17), the normal (2.18) and tangential (2.19) components of the interfacial linear momentum balance, and the interfacial energy balance (2.20) at the liquid-vapor interface, respectively, yield their dimensionless counterparts,

$$J = \frac{-u(h+s)_x + v - h_t}{\sqrt{1+\epsilon^2(h_x+s_x)^2}}, \tag{2.43}$$

$$p_v - p + 2\mathrm{Ca}\frac{u_x(h_x+s_x)^2 + \epsilon^{-2}v_y - (h+s)_x(\epsilon^{-2}u_y + v_x)}{1+\epsilon^2(h_x+s_x)^2} = \frac{(h+s)_{xx}}{(1+\epsilon^2(h_x+s_x)^2)^{3/2}}, \tag{2.44}$$

$$\frac{2\epsilon^2(h+s)_x(v_y-u_x) + (u_y+\epsilon^2 v_x)(1-\epsilon^2(h_x+s_x)^2)}{1+\epsilon^2(h_x+s_x)^2} = 0, \tag{2.45}$$

and,

$$J = -\frac{\epsilon^2(h+s)_x T_x + T_y}{(1+\epsilon^2(h_x+s_x)^2)^{1/2}}. \tag{2.46}$$

The thermodynamic-kinetic equation (2.21) for evaporative mass flux takes the dimensionless form

$$JM = \epsilon^2 N(p - p_v) + T_i - 1. \tag{2.47}$$

Dimensionless form of no-slip and no-penetration conditions on the solid-liquid interface are

$$u = 0, \qquad \text{and,} \qquad v = 0, \tag{2.48}$$

and the temperature boundary condition requires that the dimensionless temperature

$$T = T_w \tag{2.49}$$

at the solid-liquid boundary.

2.4 Lubrication approximation and evolution equation

To obtain the lubrication equations, assume that the scale L_y of the transverse variation is much smaller than its lateral counterpart L_x, so that the aspect ratio ϵ defined in (2.34) obeys

$$\epsilon \ll 1, \tag{2.50}$$

and, moreover, that the Reynolds, capillary, Péclet numbers and dimensionless number N defined in the linear momentum balance, energy balance and the thermodynamic-kinetic equation for evaporative mass flux are such that

$$\epsilon \mathrm{Re} \ll 1, \qquad \epsilon^4 \mathrm{Ca}^{-1} = 1, \qquad \epsilon \mathrm{Pe} \ll 1, \qquad \text{and} \qquad \epsilon^2 N \ll 1. \tag{2.51}$$

As will be seen in eq. (2.53) below, the second of these conditions expresses the standard lubrication theory balance between capillary pressure gradients and viscous resistance. Assume that the lateral u and transverse v components of the dimensionless fluid velocity and the dimensionless pressure p admit regular expansions in ϵ and substitute the expansions of u, v, and p into the dimensionless equations and boundary conditions. The lubrication assumptions reduces the number of governing dimensionless numbers to T_w, M, and $\theta(0)$. With above-mentioned assumptions in mind, the leading-order approximation of the dimensionless versions of governing equations and boundary conditions are derived. The leading-order approximation of the continuity equation (2.39), x-component (2.40) and y-component (2.41) of linear momentum balance and conservation of energy (2.42) inside the liquid are,

$$u_x + v_y = 0, \tag{2.52}$$

$$-p_x + u_{yy} = 0, \tag{2.53}$$

$$p_y = 0, \tag{2.54}$$

and

$$T_{yy} = 0. \tag{2.55}$$

The leading-order approximation of the interfacial mass balance (2.43), the normal (2.44) and tangential (2.45) components of the interfacial linear momentum balance, and the interfacial energy balance (2.46) at the liquid-vapor interface, respectively are

$$J + u(h+s)_x + h_t - v = 0, \tag{2.56}$$

$$p - p_v = -(h+s)_{xx}, \tag{2.57}$$

$$u_y = 0, \tag{2.58}$$

and

$$J = -T_y. \tag{2.59}$$

The leading-order approximation of the thermodynamic-kinetic equation (2.47) for evaporative mass flux takes the form of

$$JM = T_i - 1. \tag{2.60}$$

As it was mentioned earlier T_i itself is an unknown but since the temperature has a linear profile based on (2.55), to derive an expression for J independent of T_i it is advantageous to combine (2.59) with (2.60) so that

$$J = \frac{T_w - 1}{M + h}. \tag{2.61}$$

Leading-order approximations of dimensionless version of no-slip and no-penetration conditions on the solid-liquid interface are

$$u = 0, \qquad \text{and,} \qquad v = 0, \tag{2.62}$$

and the leading order approximation of the temperature boundary condition requires that the dimensionless temperature

$$T = T_w \tag{2.63}$$

along the solid-liquid interface.

It follows from the y-component (2.54) of linear momentum balance that pressure is not a function of y, thus,

$$p = p(x,t), \tag{2.64}$$

and since the pressure is known at the liquid-vapor interface by the normal (2.57) component of the interfacial linear momentum balance, the pressure is therefore known everywhere and is simply

$$p = p_v - (h+s)_{xx}. \tag{2.65}$$

Integrating the x-component (2.53) of the linear momentum balance with respect to y twice, with using the tangential (2.58) component of the interfacial linear momentum balance, and the no-slip condition (2.62a) at the solid-liquid interface gives the x-component of the fluid velocity,

$$u = \frac{p_x}{2}\big((y-s)^2 - 2(y-s)h\big). \tag{2.66}$$

Integrating the continuity (2.52) with respect to y from the solid-liquid interface, $s(x)$, to the liquid-vapor inteface, $h(x,t)+s(x)$, and using the interfacial mass balance (2.56) and no-penetration condition (2.62b) at the solid-liquid interface (with utilization of the Leibniz integral rule) gives the evolution equation,

$$h_t + \frac{1}{3}\frac{\partial}{\partial x}\left((h+s)_{xxx}h^3\right) + J = 0. \tag{2.67}$$

Finally, by substituting J from (2.61), the evolution equation for the droplet thickness takes the form of

$$h_t = -\frac{1}{3}\frac{\partial}{\partial x}\left((h+s)_{xxx}h^3\right) - \frac{T_w - 1}{M+h}, \tag{2.68}$$

where, as above,

$$M = \frac{\rho V_y \sqrt{2\pi R_M T_s}}{\rho_v \mathcal{L}}, \tag{2.69}$$

and T_w is the temperature of the solid-liquid interface scaled by the saturation temperature T_s. The first term in the right hand side of the evolution equation (2.68) which represents the capillary flux, depends on the profile of the liquid-vapor and solid-liquid interfaces. The

second term in the right hand side of the evolution equation (2.68) which represents the temperature flux, arises from that the temperature of the solid-liquid interface is higher than the saturation temperature and depends on the droplet thickness and the thermodynamic-kinematic dimensionless number M.

2.5 Initial condition and boundary conditions required to solve the evolution equation

The evolution equation for the droplet thickness

$$h_t = -\frac{1}{3}\frac{\partial}{\partial x}\left((h+s)_{xxx}h^3\right) - \frac{T_w - 1}{M + h}, \tag{2.70}$$

is a partial differential equation of 1^{st} order in time, and 4^{th} order in space; thus, one initial condition and four boundary conditions are required to determine the film thickness $h(x,t)$. In view of the assumption that the liquid layer is initially part of a cylinder with circular cross-section, the initial profile of the liquid-vapor interface is a circular cap with its center located on the symmetry line in a way that the required initial contact angle $\theta(0)$, shown in Figure 2.3, is achieved.

Granted that the problem is symmetric and assuming that the first and third derivatives of the solid-liquid profile $s(x)$ at the location of symmetry line vanish, the symmetric boundary conditions require that

$$h_x(0,t) = 0, \qquad \text{and,} \qquad h_{xxx}(0,t) = 0. \tag{2.71}$$

In addition to the two symmetric conditions at $x = 0$, two other conditions are required to solve the evolution equation (2.70); these two conditions which, are applied at the contact line and therefore are referred to as the contact line conditions, are provided separately for the cases of pinned and moving contact lines in following subsections.

2.5.1 Contact line conditions for the pinned contact line case

For the case in which the contact-line is pinned i.e. the wetted radius is constant, the x-component $r(t)$ of the contact line position shown in Figure 2.3 is known and is not changing

with time such that

$$r(t) = 1. \tag{2.72}$$

The first contact line condition is that the droplet thickness at the location of the contact line vanishes, thus

$$h(1,t) = 0. \tag{2.73}$$

To produce the second contact line condition, it is assumed that at the location of the contact line the liquid pressure p is in equilibrium with the vapor pressure p_v, i.e. there is no pressure driven flow into the contact line itself. Thus, using (2.57) it follows that

$$h_{xx}(1,t) + s_{xx}(1) = 0. \tag{2.74}$$

A summary of the evolution equation, initial condition and boundary conditions required to analyze the evaporation of a symmetric droplet on a curved solid substrate for the case in which, the contact line is pinned and the contact angle can change, is provided below

- The evolution equation:

$$h_t = -\frac{1}{3}\frac{\partial}{\partial x}\Big((h+s)_{xxx}h^3\Big) - \frac{T_w - 1}{M+h}. \tag{2.75}$$

- Initial condition:

$$h_{xxx}(x,0) = 0. \tag{2.76}$$

- Symmetry conditions:

$$h_x(0,t) = 0, \qquad \text{and,} \qquad h_{xxx}(0,t) = 0. \tag{2.77}$$

- Contact line conditions:

$$h(1,t) = 0, \qquad \text{and,} \qquad h_{xx}(1,t) + s_{xx}(r_o) = 0. \tag{2.78}$$

2.5.2 Contact line conditions for the moving contact line case

For the case of the moving contact line, following that the liquid thickness is equal to zero at the contact line, the first contact line condition is

$$h(r(t), t) = 0. \tag{2.79}$$

The second contact line conditions, the condition of no capillary flow into the contact line, requires that

$$h_{xx}(r(t), t) + s_{xx}(r(t)) = 0. \tag{2.80}$$

Since the location of contact line is not known in advance for this mode of evaporation, the two contact line conditions are no longer sufficient to solve the evolution equation and therefore an additional condition is required. To provide this additional condition, it is assumed that while the wetted radius $r(t)$ is changing over time, the value of contact angle $\theta(t)$ remains constant such that

$$\theta(t) = \theta_o. \tag{2.81}$$

Thus, during the evaporation process the contact line is allowed to slip and its location is chosen so that the contact angle remains constant and equal to its initial value θ_o. Thus, the slope of liquid-vapor interface at the contact line obeys

$$h_x(r(t), t) = \Theta_o. \tag{2.82}$$

This condition serves as the additional contact line condition required to solve the problem for the moving contact line case. Here as a result of the lubrication theory scaling, Θ_o is the scaled contact angle ($\Theta_o = -\theta_o/\epsilon$); for a comprehensive explanation of the scaled contact angle see Moyle et al [16].

A summary of the evolution equation, initial condition and boundary conditions required to analyze the evaporation of a symmetric droplet on a curved solid substrate for the case in which, the contact is moving and the contact angle remains constant is provided below

- The evolution equation:

$$h_t = -\frac{1}{3}\frac{\partial}{\partial x}\left((h+s)_{xxx}h^3\right) - \frac{T_w - 1}{M+h}. \tag{2.83}$$

- Initial condition:

$$h_{xxx}(x,0) = 0. \tag{2.84}$$

- Symmetry conditions:

$$h_x(0,t) = 0, \qquad \text{and,} \qquad h_{xxx}(0,t) = 0. \tag{2.85}$$

- Contact line conditions:

$$h(r(t),t) = 0, \qquad h_{xx}(r(t),t) + s_{xx}(r(t)) = 0, \qquad \text{and,} \qquad h_x(r(t),t) = \Theta_o. \tag{2.86}$$

Chapter 3

NUMERICS

3.1 Applying method of lines to solve the initial/boundary value problem

As we have seen, the evaporation of a droplet on a curved solid substrate is governed by the following intial-boundary value problem

$$h_t = -\frac{1}{3}\frac{\partial}{\partial x}\big((h+s)_{xxx}h^3\big) - \frac{T_w - 1}{M+h}. \tag{3.1}$$

The initial profile is assumed to be circular and the boundary conditions are symmetry conditions

$$h_x(0,t) = 0, \qquad \text{and,} \qquad h_{xxx}(0,t) = 0, \tag{3.2}$$

which are identical for both cases of pinned and moving contact lines, and the contact line conditions, which are provided separately for each evaporation mode,

I) Contact line conditions for the pinned contact line case:

$$h(1,t) = 0, \quad \text{and,} \quad h_{xx}(1,t) + s_{xx}(1) = 0. \tag{3.3}$$

II) Contact line conditions for the moving contact line case:

$$h(r(t),t) = 0, \quad h_{xx}(r(t),t) + s_{xx}(r(t)) = 0, \quad \text{and,} \quad h_x(r(t),t) = \Theta_o. \tag{3.4}$$

Since the problem is nonlinear, a numerical algorithm is required to solve the evolution equation subject to the initial condition and boundary conditions. For both cases of pinned and moving contact lines, the method of lines is chosen as the numerical technique to solve the initial-boundary value problem. The method of lines is used to discretize the PDE in space, transforming it into a system of ordinary differential equations in time. These are

then solved using the MATLAB stiff solver ode15s. Solutions achieved by `ode23s`, which computes the Jacobian with a different algorithm compared to `ode15s`, were found to be in good agreement with the ones produced by ode15s. It is observed that for some intervals of time, to solve (3.1) the numerical method must take excessively small time steps to obtain satisfactory results and therefore using a stiff solver is found to be necessary. For all cases in this work the initial spatial mesh size, is chosen to be around 0.01. The size of time step, which may change from case to case, is taken to be small enough such that with 50% change in the spatial step size the solution changes no more than 0.1%.

3.2 Discretization of the evolution equation and symmetry conditions

Centered finite difference schemes are utilized to discretize the evolution equation in space and therefore the computational domain is divided into n intervals with $n+1$ nodes in the x direction. As shown in Figure 3.1 the first node is located on the symmetry line and the $(n+1)$-th node specifies the contact line. To evaluate the droplet thickness $h(x,t)$ over time, the right hand side of (3.1)

$$-\frac{1}{3}\frac{\partial}{\partial x}\big((h+s)_{xxx}h^3\big) - \frac{T_w-1}{M+h} \tag{3.5}$$

is discretized. The third derivative $(h+s)_{xxx}$ term is computed centered between mesh points and therefore the term $(h+s)_{xxx}h^3$ is computed at the midpoint between $(i+1)$-th and i-th and between i-th and $(i-1)$-th nodes respectively. Thus, at any time level m, (3.5) is discretized in space in the following fashion

$$-\frac{1}{3}\left(\frac{f^m_{i+1/2}(g^m_{i+2}-3g^m_{i+1}+3g^m_i-g^m_{i-1})}{(\Delta x^m)^3} - \frac{f^m_{i-1/2}(g^m_{i+1}-3g^m_i+3g^m_{i-1}-g^m_{i-2})}{(\Delta x^m)^3}\right)\frac{1}{(\Delta x^m)} - \frac{T_w-1}{M+h^m_i}. \tag{3.6}$$

Here Δx^m represents the uniform distance between each two nodes at time step m. h^m_i denotes the thickness of droplet $h(x,t)$, g^m_i the y-component, $h(x,t)+s(x)$, of the liquid-

vapor interface, and $f^m_{i\pm1/2}$ the averages of $(g^m_i)^3$ over adjacent nodes, as defined by

$$f^m_{i\pm1/2} = \frac{(g^m_i)^3 + (g^m_{i\pm1})^3}{2}, \tag{3.7}$$

all at the i-th spatial node and time step m. Δx^m, h^m_i, and g^m_i are shown in Figure 3.1. Evaluating (3.6) for $i = 3, 4 \cdots$, and $n-2$ is straightforward but to evaluate the right hand

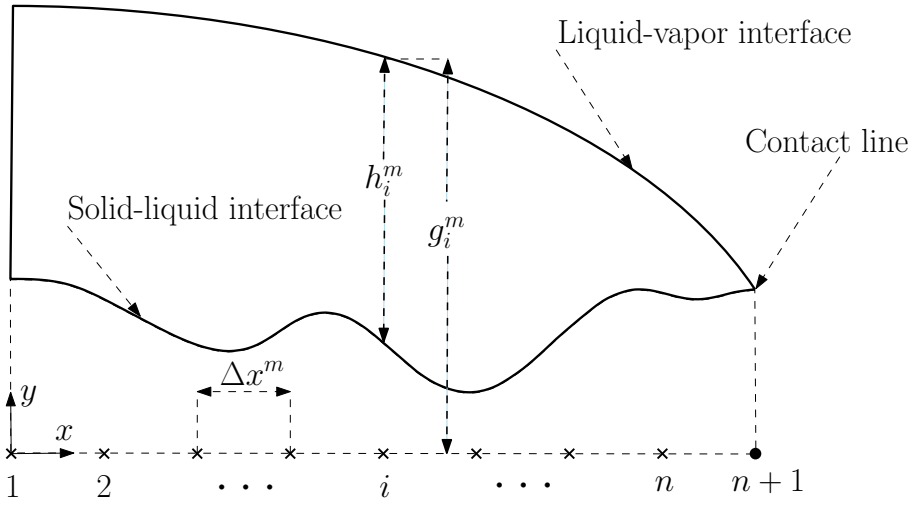

Figure 3.1: Schematic of the computational domain at a given time-step.

side of the evolution equation for $i = 1, 2, n-1$, and n it is required to use the boundary conditions.

To evaluate the right hand side of the evolution for $i = 1$ and 2 values of g^m_i are required to be known on ghost nodes $i = 0$ and $i = -1$. Applying the 2^{nd} order accurate central finite difference scheme to symmetry conditions (3.2.a) and (3.2.b) requires that

$$h^m_0 = h^m_2, \qquad \text{and,} \qquad h^m_{-1} = h^m_3, \tag{3.8}$$

and since the first $s_x(0)$ and third derivative $s_{xxx}(0)$ of solid-liquid height is taken to be zero at the the symmetry location, values of g^m_i for $i = 0$ and $i = -1$ become

$$g^m_0 = g^m_2, \qquad \text{and,} \qquad g^m_{-1} = g^m_3. \tag{3.9}$$

To evaluate the right hand side of the evolution for $i = n - 1$ and $i = n$ the boundary conditions at the contact line must be applied.

3.3 Numerical techniques to apply the contact line conditions

The required values of g_i^m for $i = n + 1$ and $i = n + 2$ are provided by utilizing the contact line conditions. Since the contact line conditions are different for pinned and moving contact lines, the numerical analysis of satisfying the contact line conditions is explained separately for each case.

For the case of pinned contact line, since the wetted radius remains constant over time the problem is a static boundary problem. Thus, once the required values of g_i^m for $i = n+1$ and $i = n + 2$ are provided the droplet thickness can be evaluated by integrating (3.6) over time. The value of g_i^m for $i = n + 1$ is simply provided by the first contact line condition (3.3.a) as

$$g_{n+1}^m = s_{n+1}, \tag{3.10}$$

where s_{n+1} denotes the height of the solid-liquid interface at the location of contact line. Since the contact line is stationary and the solid-liquid interface is not changing over time, s_{n+1} is constant over time. Moreover, using 2^{nd} order accurate central finite difference scheme, the second contact line condition (3.3.b) is discretized to provide the value of g_i^m for $i = n + 2$ as

$$g_{n+2}^m = 2g_{n+1}^m - g_n^m. \tag{3.11}$$

In summary, the discretized evolution equation (3.6), accompanied with the discretized symmetry conditions, (3.9.a) and (3.9.b), and contact line conditions, (3.10) and (3.11), provide the sufficient basis to integrate the evolution equation in time. As a result of the integration the droplet thickness $h(x, t)$ is determined. Once $h(x, t)$ is known the evaporative mass flux $J(x, t)$ and contact angle $\theta(t)$ are computed as secondary quantities.

For the case of moving contact line, the first contact line condition (3.4.a) provides the required value of g_i^m for $i = n + 1$ as

$$g_{n+1}^m = s_{n+1}, \tag{3.12}$$

where s_{n+1} denotes the height of the solid-liquid interface at the location of contact line. The second contact line condition (3.4.b) provides the value of g_i^m for $i = n + 2$ as

$$g_{n+2}^m = 2g_{n+1}^m - g_n^m. \tag{3.13}$$

Since the wetted radius is changing over time, the location of contact line is no longer known beforehand and therefore the problem of moving contact line is a moving boundary problem. Consequently, to evaluate the right hand side of the evolution equation through (3.6) for $i = 1, 2, \cdots, n$, it is also required to evaluate the location of the contact line, i.e the wetted radius $r(t)$. Thus, an operator splitting technique with two stages is utilized to simultaneously evaluate the droplet thickness $h(x, t)$ and the location of contact line.

In the first stage, the evolution equation is solved assuming the position of the contact line is unchanged. The resulting solution will violate the condition of fixed contact angle, thus requiring an iteration to find the position of the contact line consistent with the initial value of the contact angle. The yellow curve in Figure 3.2 illustrates the situation after the first stage.

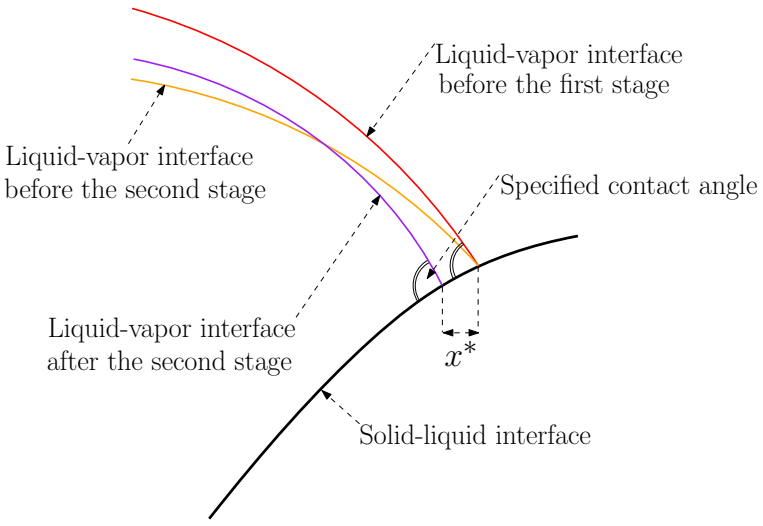

Figure 3.2: Schematic of liquid-vapor interface at different stages of operator splitting method for the moving contact line case.

In the second stage, the contact line is moved a distance x^* sufficient to regain the specified contact angle. To evaluate x^*, the interface is described near the contact line using the Lagrange interpolating polynomial with three points. The slope of the interface at the contact line is then calculated from this polynomial implicitly as a function of the new position x^*. Next, an iteration scheme is used to evaluate x^* based on the calculated slope of the liquid-vapor interface as a function of x^* and the slope $s_x(x^*)$ of the solid-liquid interface at the contact line location.

For the case where the solid-liquid interfaces flat, this procedure produces a quadratic equation for the slope which can be solved analytically for x^*. When a curved substrate is involved, an iteration is required to find the new position x^*. The purple curve in Figure 3.2 illustrates the situation after the second stage. Thus, the droplet thickness and the wetted radius are determined simultaneously. Once the new position of the contact line is determined, the computational domain is remeshed and the values of h are evaluated on the new mesh by spline interpolation. The number of nodes and consequently the distance (Δx^m) between each two nodes is chosen such that at any time step the distance x^* that contact line moves is smaller than $(\Delta x^m)/2$. Also, an iterative method is employed to choose the size of the time step in the first stage such that all boundary conditions are satisfied to a specified accuracy at the end of the second stage (the contact angle equals the specified value with less than 5% error).

This process is then repeated until the specified time is reached and thus the droplet thickness $h(x,t)$ and wetted radius $r(t)$ are determined simultaneously. Once $h(x,t)$ and $r(t)$ are known the evaporative mass flux $J(x,t)$ is computed as a secondary quantities.

Chapter 4

EVAPORATION OF DROPLET ON FLAT SOLID SUBSTRATES

In this chapter, the evolution equation (2.70) is solved for the case in which the solid substrate is flat, as shown in Figure 4.1. Since the substrate is flat, $s(x)$ and all its derivatives are identically zero. Hence, for the flat solid-liquid interface the evolution equation (2.70) is simplified to

$$h_t = -\frac{1}{3}\frac{\partial}{\partial x}(h_{xxx}h^3) - \frac{T_w - 1}{M + h}. \tag{4.1}$$

Following the numerical analysis provided in Chapter 3, the simplified evolution equation (4.1) is solved separately for pinned and moving contact line scenarios. For the pinned contact line case, the quantities of interest are the droplet thickness $h(x,t)$, evaporative mass flux $J(x,t)$, and contact angle $\theta(t)$. For the moving contact line case, the quantities are $h(x,t)$, $J(x,t)$ and the wetted radius $r(t)$. The solution for these quantities rely on the initial profile of the droplet and the dimensionless parameters of the problem, i.e. the initial contact angle $\theta(0)$, M and T_w. Thus, the problem is solved for a range of M, T_w, and, $\theta(0)$

$$\begin{cases} \theta(0) = 5^o, \quad \text{and} \quad 10^o, \\ \text{M} = 1, \quad 2, \quad 3, \quad 4, \quad \text{and} \quad 5, \\ T_w = 1.1, \quad 1.2, \quad 1.3, \quad \text{and} \quad 1.4. \end{cases}$$

separately for each evaporation mode.

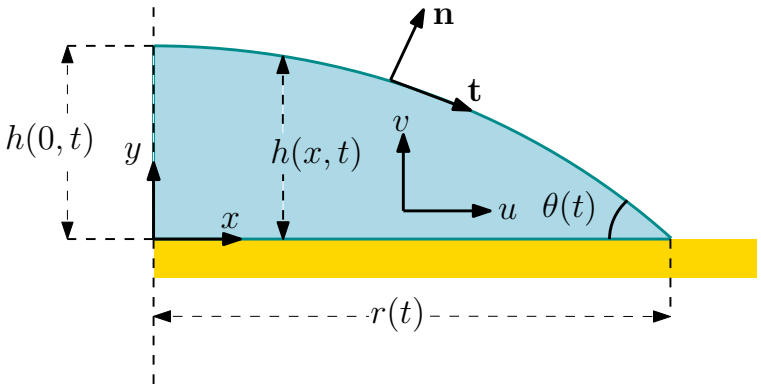

Figure 4.1: 2D Schematic of a liquid droplet on a flat solid substrate

4.1 Evaporation of droplets on flat solid substrates with pinned contact lines

For the case in which the contact line is pinned, i.e. $r(t) = 1$, the evolution equation (4.1) is numerically solved for the circular cap initial condition and based on the symmetry conditions and contact line conditions, respectively presented below

$$\left.\begin{array}{c} h_{xxx}(x,0) = 0 \\ h_x(0,t) = 0, \text{ and, } h_{xxx}(0,t) = 0, \\ h(1,t) = 0, \text{ and, } h_{xx}(1,t) = 0. \end{array}\right\}$$

As a reference case, we consider the set of parameters $M = 2$, $T_w = 1.2$ and $\theta(0) = 5^o$ and show the droplet thickness $h(x,t)$, evaporative mass flux $J(x,t)$, and contact angle $\theta(t)$ in Figures 4.2-4.4.

As shown in Figure 4.2 both the thickness $h(0,t)$ of the droplet at the symmetry node and the contact angle $\theta(t)$ are decreasing in time.

Figure 4.3 shows a plot of the evaporative flux distribution. As seen, the flux is always positive, indicating evaporation, and increases with time as the thermal resistance decreases with decreasing thickness. Finally, as expected the flux is a maximum at the contact line, since the thickness is a minimum there. These simulations have been done over a the range of M and T_w indicated above, but will not be shown, as the results for $h(x,t)$ and $J(x,t)$

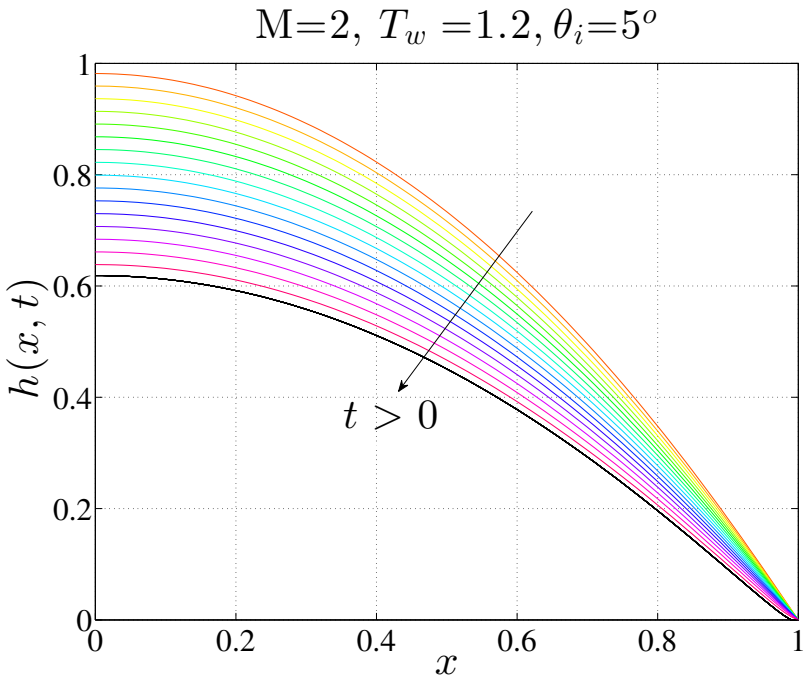

Figure 4.2: $h(x,t)$ for the case of $M = 2$, T_w, $\theta(0) = 5^o$ with pinned contact line on a flat solid substrate.

are qualitatively similar to those in Figures 4.2 and 4.3.

The more interesting quantity is the contact angle and its dependence on time. Figure 4.4 reveals that the contact angle $\theta(t)$ is decreasing over time during the evaporation process. As shown in Figure 4.4, the contact angle decreases almost linearly for a range of time until time reaches to a value, which we refer to as critical time t_{cr}, at which the dynamics becomes much faster and thus, the value of the contact angle starts to drop rapidly until the local contact angle goes to zero. Figure 4.5, which shows the results of $h(x,t)$ near the contact line, indicates how this happens in advance of the total evaporation. The solution after t_{cr} requires a change in our basic modeling assumptions which we do not pursue in this work, but we conclude that at this instant the contact line depins and the droplet starts to evaporate consistent with the onset of the third mode of evaporation, mentioned in the Introduction,

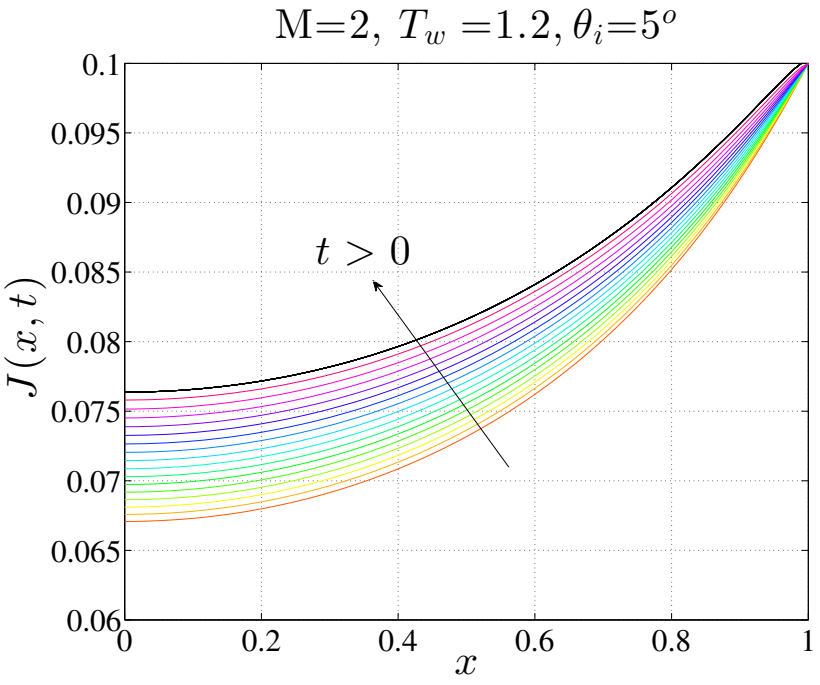

Figure 4.3: Evaporative mass flux $J(x,t)$ for the case of $M = 2$, T_w, $\theta(0) = 5^o$ with pinned contact line on a flat solid substrate.

i.e. both $\theta(t)$ and $r(t)$ decrease until the entire liquid is evaporated.

We found that locally near the location of the contact line the solution for $h(x,t)$ is dependent on the spatial mesh size and as a result of that $\theta(t)$ and consequently t_{cr} are also mesh-dependent. Figure 4.6 shows how the contact angle $\theta(t)$ varies for different number of spatial nodes. This mesh-dependency is larger for larger values of T_w and smaller values of M. In order to understand this mesh dependence, we computed the derivatives of the solution and found that the profiles of h_{xx} are very steep near the contact line as the solution develops an inflection point. Thus a spatial boundary layer in h_{xx} develops near the contact line. We believe that the mesh dependence occurs as a result of our use of uniform mesh, which requires many points in order to resolve this boundary layer. To find a mesh-independent value for t_{cr}, we decided to calculate the value of t_{cr} for the case in which the number of

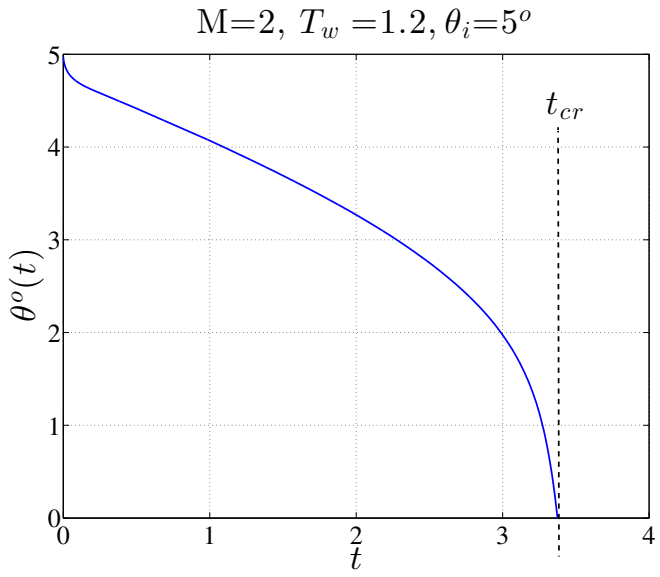

Figure 4.4: Contact angle $\theta(t)$ for the case of $M = 2$, T_w, $\theta(0) = 5^o$ with pinned contact line on a flat solid substrate.

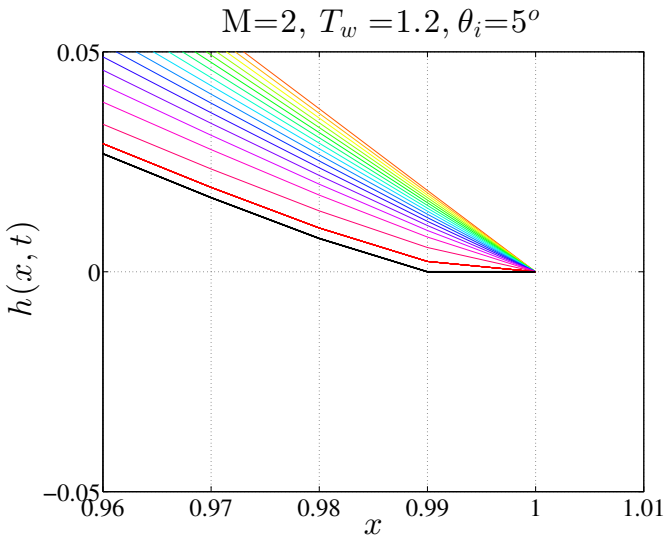

Figure 4.5: Results of $h(x,t)$ for the case of $M = 2$, $T_w = 1.2$, $\theta(0) = 5^o$ near the contact line. The curve shown in black shows the solution at the critical time t_{cr}.

spatial nodes $N \to \infty$, i.e. the spatial mesh size $\Delta x \to 0$. We emplyed a two-step fitting and extrapolation process to achieve this goal. First, we apply a second order polynomial fit to the values of t_{cr} calculated for different cases of Δx. Next using extrapolation, we calculate t_{cr} for the spatial mesh size $\Delta x \to 0$. To ensure the mesh-independency of the final result of this process, we calculated the contact angle via second order and fourth order backward finite difference methods and applied the fitting and extrapolation process to the values of t_{cr} calculated based on both methods. Our results, shown in Figure 4.7, indicate that the final calculated value of t_{cr} corresponding to $\Delta x \to 0$ is approximately the same for both of these methods.

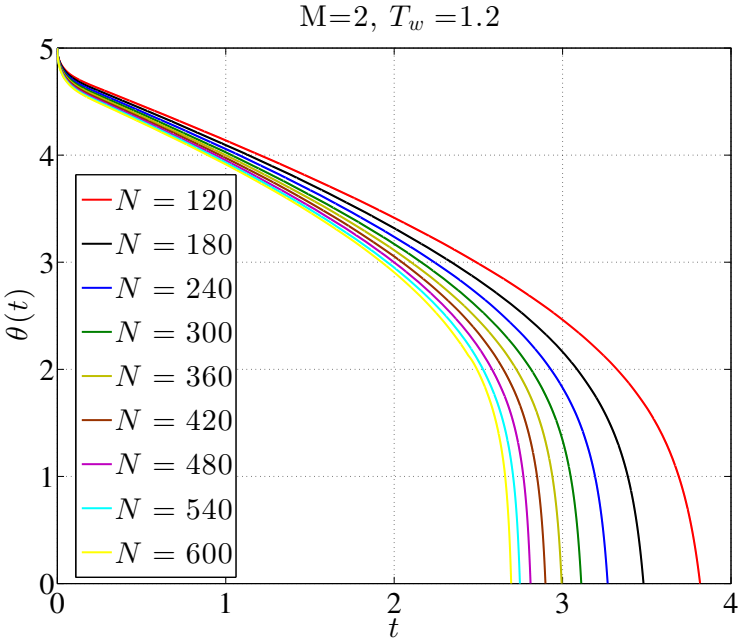

Figure 4.6: Results of $\theta(t)$ for different values of N indicating that $\theta(t)$ is mesh-dependent.

To produce the mesh-independent contact angle $\theta(t)$ for $0 \leq t \leq t_{cr}$, we apply the same polynomial fitting and extrapolation technique we used to find t_{cr} for $\Delta x \to 0$. First, We pick some values of θ between 0 and $\theta(0)$ and then for each Δx, we find the time that it takes for the contact angle to reach to each of these θ-values. Next, we apply a second order

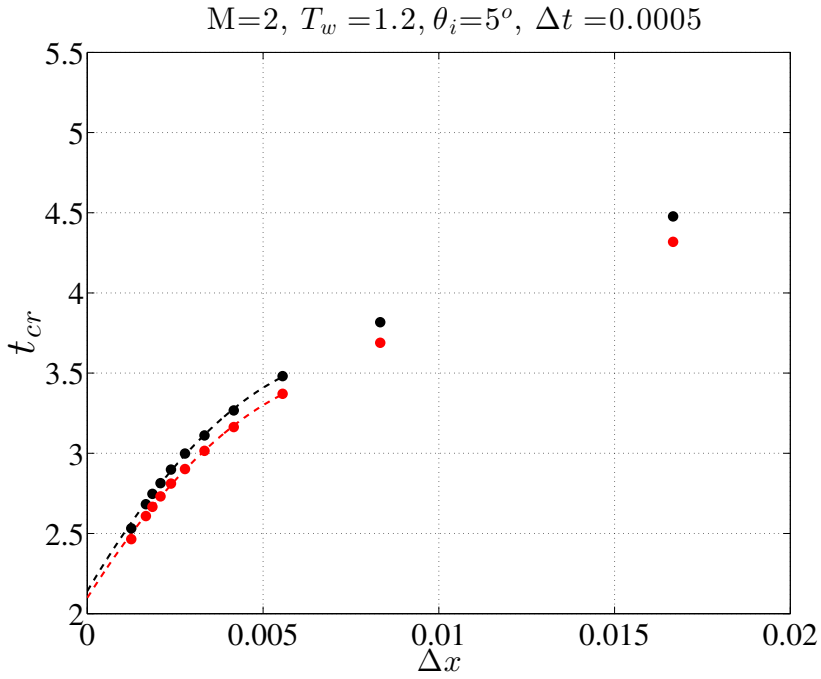

Figure 4.7: Fitting and extrapolation technique applied to the values of t_{cr} generated for different values of Δx. Black and red colors, respectively, correspond to the contact angle calculated based on the second order and fourth order backward finite difference methods. Dashed lines correspond to second order polynomial fits for each case. The intersection of the dashed lines and the vertical axis results the calculated mesh-independent value for t_{cr}. For both cases, the first two data points on the right, associated with larger values of Δx are not used in the fitting process to achieve higher levels of accuracy.

polynomial fit to the calculated time values for each θ, and using extrapolation, calculate the time corresponding to $\Delta x \to 0$. Finally, we use the time values calculated for $\Delta x \to 0$ to generate $\theta(t)$ for $\Delta x \to 0$. By increasing the number of chosen θ-values we are able to calculate $\theta(t)$ with higher resolution. The black curve shown in Figure 4.8 is the final product of this process. We generated the mesh-independent version of the contact angle $\theta(t)$ over a range of M, T_w and $\theta(0)$ indicated above and found that the polynomial fitting

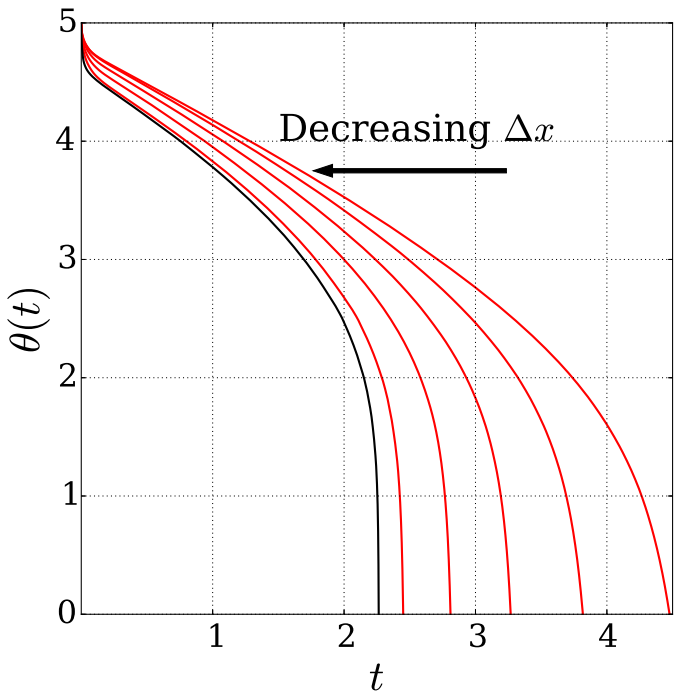

Figure 4.8: Black curve indicates the calculated $\theta(t)$ for $\Delta x \to 0$ by applying the extrapolation and fitting technique to 1001 values of θ between 0 and 5 degrees. The red curves correspond to generated $\theta(t)$ with different values of Δx. The values of Δx associated with the red curves are: $1/60, 1/120, 1/240, 1/480, and 1/960$.

and extrapolation technique solves the problem of mesh dependency for $\theta(0) = 5, 10$ degrees, $1.1 \leq T_w \leq 1.4$ and $2 \leq M \leq 5$. However, for the case of $M = 1$ and specially for larger values of T_w the mesh-dependency is too large to be solved by this technique. Note that as of this point, whenever we refer to $\theta(t)$ or t_{cr} we mean the reliable, mesh-independent version calculated for $\Delta x \to 0$.

In general, the critical time t_{cr} may depend on the initial contact angle $\theta(0)$, T_w and M. To investigate this dependency we generated the contact angle $\theta(t)$, for cases of $\theta(0) = 5, 10$ degrees, some values of T_w in $1.1 \leq T_w \leq 1.4$ and $M = 2, 3, 4$, and 5. Figure 4.9 shows the contact angle as a function of time for the sample case with $T_w = 1.2$ and different

values of M. Results for other values of T_w will not be shown since they are qualitatively similar to Figure 4.9 when plotted as a function of time t. Based on our results, shown in 4.10a and 4.10b, we conclude that for the range of initial contact angle $\theta(0)$ we studied, the dependency of t_{cr} on $\theta(0)$ is very weak and also that the critical time t_{cr} is a nonlinearly decreasing function of T_w and a linearly increasing function of M.

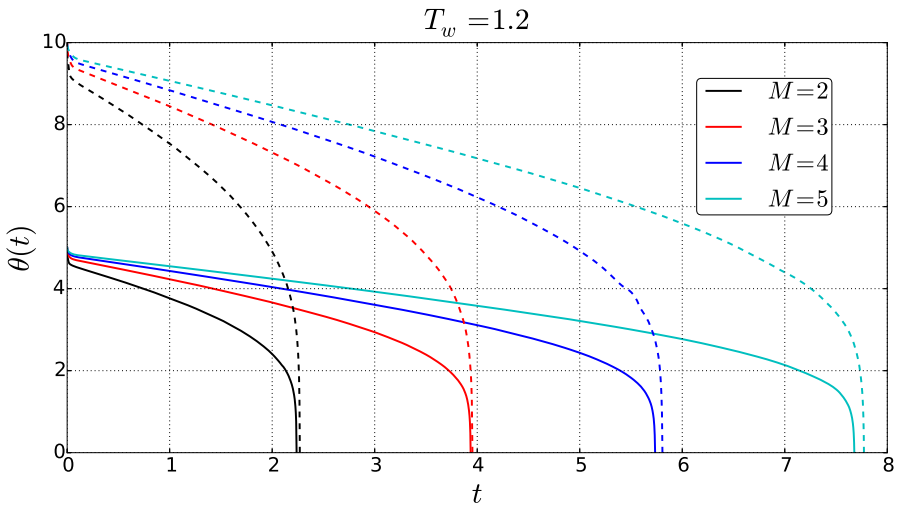

Figure 4.9: The contact angle $\theta(t)$ for different values of M, for the case of $T_w = 1.2$. The solid lines and the dashed lines, respectively, show the results for the case of $\theta(0) = 5^o$ and $\theta(0) = 10^o$.

As shown in Figure 4.9, the general shape of the curves are similar near t_{cr}. We observed that once time is rescaled as $(t_{cr} - t)/M^p$, $\theta(t)/\theta(0)$ corresponding to different values of M collapse into each other as time approaches t_{cr}. The effect of such scaling is shown in Figure 4.11 for the reference case of $T_w = 1.2$ with p chosen as 1.55. We found that such scaling can be achieved for p between 1.4 and 1.6, for all values of T_w that we studied. These results clearly suggest self- similarity in M but attempts to analytically describe the final approach to the singularity proved unsuccessful, so we leave this for later work.

Our result for the case of pinned contact line on flat substrates reveal that due to the

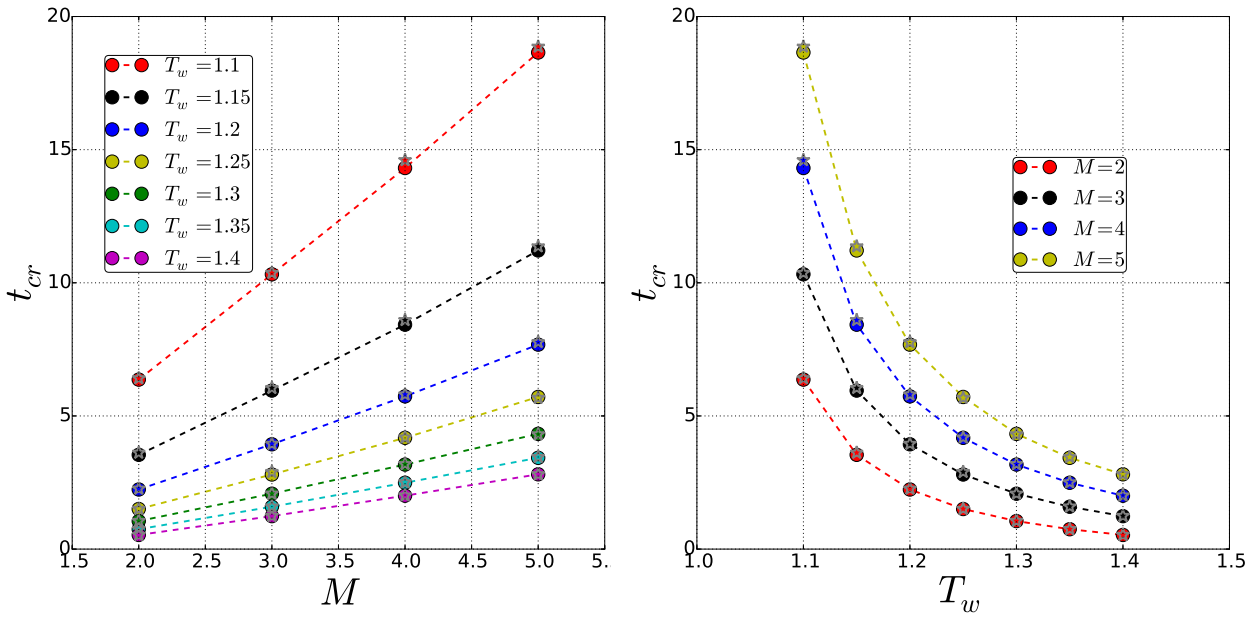

(a) (b)

Figure 4.10: (a) t_{cr} as a function of M for different values T_w indicating that for any given T_w, t_{cr} is a linearly increasing function of M. (b) Results of t_{cr} as a function of T_w for different values M indicating that for any given M, t_{cr} is a non-linearly decreasing function of T_w. In both (a) and (b) circles correspond to the results for $\theta(0) = 5^o$ and star signs correspond to the results for $\theta(0) = 10^o$. The small distances between the circles and star signs reveal that the dependence of t_{cr} on the initial contact angle is very weak

evaporation the droplet loses mass and therefore both the droplet thickness $h(x,t)$ and contact angle $\theta(t)$ decreases over time. At first, the contact angle decreases almost linearly for a range of time. With decreasing $h(x,t)$ and $\theta(t)$ over time the thermal resistance decreases and thus the evaporative mass flux increases. As the total evaporative mass flux increases the evaporation process becomes faster over time; as the time approaches a certain value the contact angle no longer follows the linear manner and starts to drop rapidly, until it

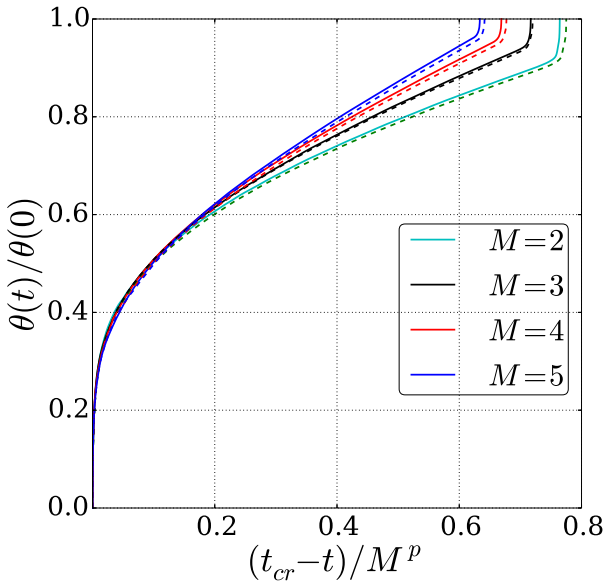

Figure 4.11: The contact angle $\theta(t)$ as a function of $(t_{cr} - t)/M^p$ for the case of $T_w = 1.2$ and $p = 1.55$. The solid and the dashed lines show the results for the case of $\theta(0) = 5^o$ and $\theta(0) = 10^o$, respectively.

becomes zero at a critical time t_{cr}. This happens at a finite time and in advance of the total evaporation; hence, we conclude that the $\theta \to 0$ does not correspond to dry out and that it may signal depinning. We believe that after t_{cr} the evaporation may change to the third mode of evaporation, in which both the contact angle and wetted radius vary. Moreover, for all studied values of T_w when time approaches t_{cr} the contact angle scaled by its initial value illustrates self-similarity in M and thus can be described via an asymptotic scaling law. It is also observed that the value of t_{cr} is larger for larger values of M and/or smaller values of T_w. This aligns with (2.61) which indicates that J is directly proportional to T_w and inversely proportional to M.

4.2 Evaporation of droplets on flat solid substrates with moving contact lines

For the case in which the contact line recedes while the contact angle is fixed to be constant, i.e. $\theta(t) = \theta(0) = \theta_o$, the evolution equation (4.1) is solved numerically based on the circular cap initial condition, symmetry conditions and contact line conditions,

$$\left.\begin{array}{c} h_{xxx}(x,0) = 0 \\ h_x(0,t) = 0, \text{ and, } h_{xxx}(0,t) = 0, \\ h(r(t),t) = 0, \; h_{xx}(r(t),t) = 0, \text{ and, } h_x(r(t),t) = \Theta_o. \end{array}\right\}$$

For the reference set of parameters $M = 2$, $T_w = 1.2$ and $\theta(0) = 10^o$ the droplet profile, evaporative mass flux and wetted radius are shown in Figures 4.12-4.15.

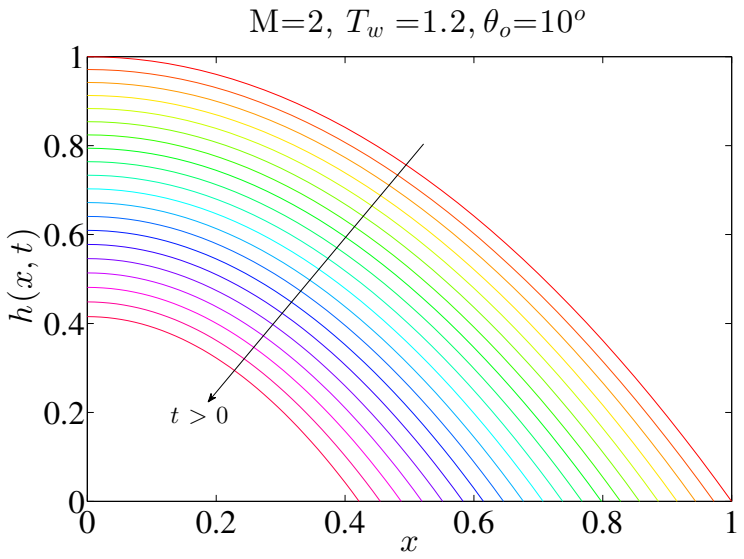

Figure 4.12: The droplet thickness $h(x,t)$ for the case of $M = 2$, T_w, and $\theta(0) = 10^o$ with moving contact line evaporating in constant contact angle mode on a flat solid substrate.

As shown in Figure 4.12 both the thickness $h(0,t)$ of the droplet at the symmetry node and wetted radius $r(t)$ are decreasing in time while the contact angle is fixed to be constant.

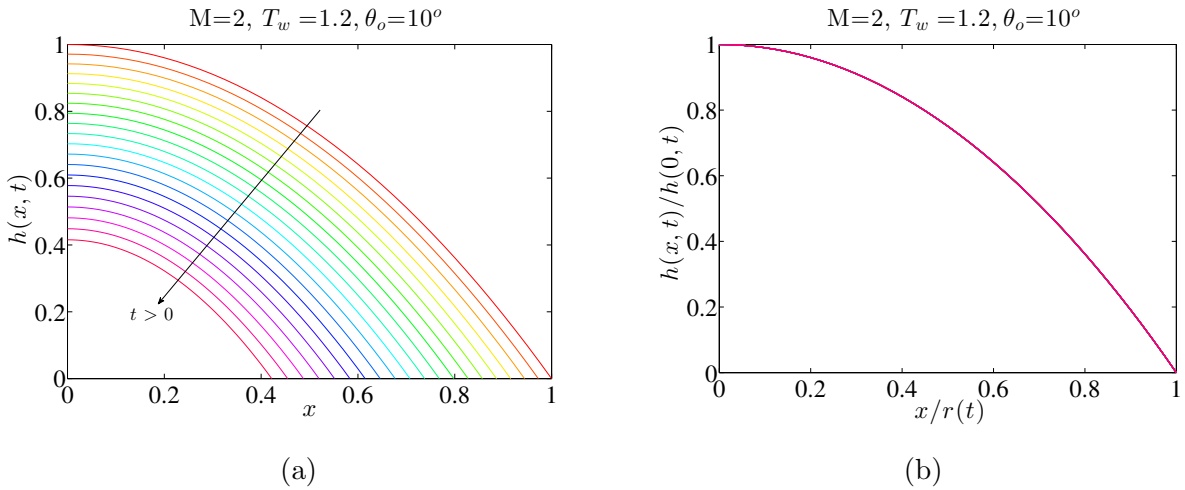

(a) (b)

Figure 4.13: (a) The droplet thickness $h(x,t)$ vs x over time. (b) Results of droplet thickness $h(x,t)/h(0,t)$ scaled by its maximum vs $x/r(t)$.

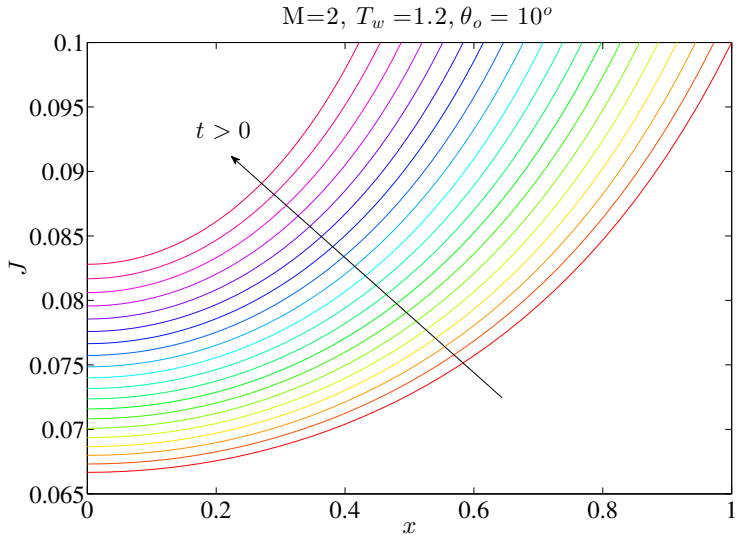

Figure 4.14: The evaporative mass flux $J(x,t)$for the case of $M = 2$, T_w, and $\theta(0) = 10^o$ with moving contact line evaporating in constant contact angle mode on a flat solid substrate.

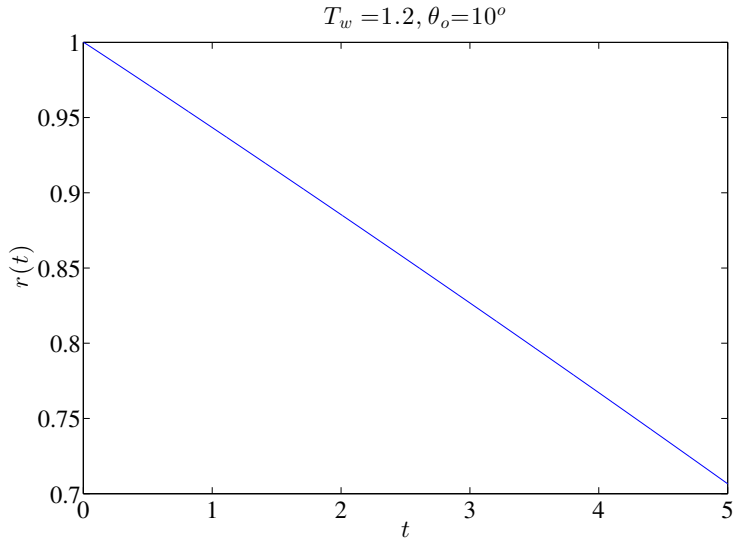

Figure 4.15: The wetted radius $r(t)$ for the case of $M = 2$, T_w, and $\theta(0) = 10^o$ with moving contact line evaporating in constant contact angle mode on a flat solid substrate.

Figure 4.12 also indicates that $h(x,t)$ retains a nearly constant shape, consistent with the static solution of constant curvature. This suggests that $h(x,t)$ can be scaled by its maximum value at the centerline and x scaled by the instantaneous value of $r(t)$. Figure 4.13 shows the result of this rescaling: the profiles collapse onto a single curve, indicating that the initial liquid-vapor interface does keep its initial circular cap shape as it evaporates. Hence, for the evaporation on flat substrates with moving contact line and fixed contact angle, our results validates previous analyses, mentioned in the Introduction, which *assume* that the droplet cross section remains circular during the evaporation.

As indicated by Figure 4.14 the evaporative mass flux J always has its maximum at the contact location while it is increasing everywhere over time (except at the contact line location where h vanishes and thus the value of J is maximum and constant). The behavior of $J(x,t)$ is verified by (2.61)

$$J = \frac{T_w - 1}{M + h},$$

and is similar to the pinned case except that for the moving contact line case the contact

line location i.e. the location at which J is maximum, is no longer fixed in time.

Simulating $h(x,t)$ and $J(x,t)$ for different values of M and T_w reveals that while the evaporation process is faster for smaller values of M and/or larger values of T_w, plots of droplet profile $h(x,t)$ and evaporation mass flux $J(x,t)$ are qualitatively similar to 4.12 and 4.14. Due to this similarity the results of these simulations will not be presented.

Figure 4.15 reveals that the wetted radius $r(t)$ is decreasing almost linearly over time during the evaporation process suggesting the contact line is moving with approximately constant speed. Such behavior is expected for a droplet with small contact angle, especially when M dominates h. The leading order terms in the balance between the rate of change of volume and the total evaporative flux integrated along the interface (which scales with r) indicate that $d(r^2)/dt \propto -r$ and thus rationalize the linear decrease of $r(t)$ over time. Figures 4.16 and 4.17 show that the contact line moves with an approximately constant speed for all values of examined parameters, M, T_w and $\theta(0)$, mentioned earlier in this chapter. Moreover, we found that the speed u_{cl} of contact line is almost independent of θ_o, is a linearly increasing function of T_w, and is a nonlinearly decreasing function of M. The latter two observations are illustrated in Figure 4.18.

In conclusion, as a result of mass loss due to the evaporation, both the droplet thickness $h(x,t)$ and wetted radius $r(t)$ decrease over time in a fashion that the droplet retains a nearly constant shape consistent with the static solution of constant curvature. Our results also show that during the evaporation process the contact line recedes in a nearly constant speed. This can indicate that although decreasing $h(x,t)$ increases the value of evaporative mass flux $J(x,t)$ over time but with decreasing $r(t)$ the total evaporative mass flow rate and the total area of the droplet change in a manner that the contact line moves with a nearly constant speed during the whole process. Finally, as could be predicted qualitatively by (2.61), we found that the contact line speed u_{cl} is a linearly increasing function of T_w and a nonlinearly increasing function of M.

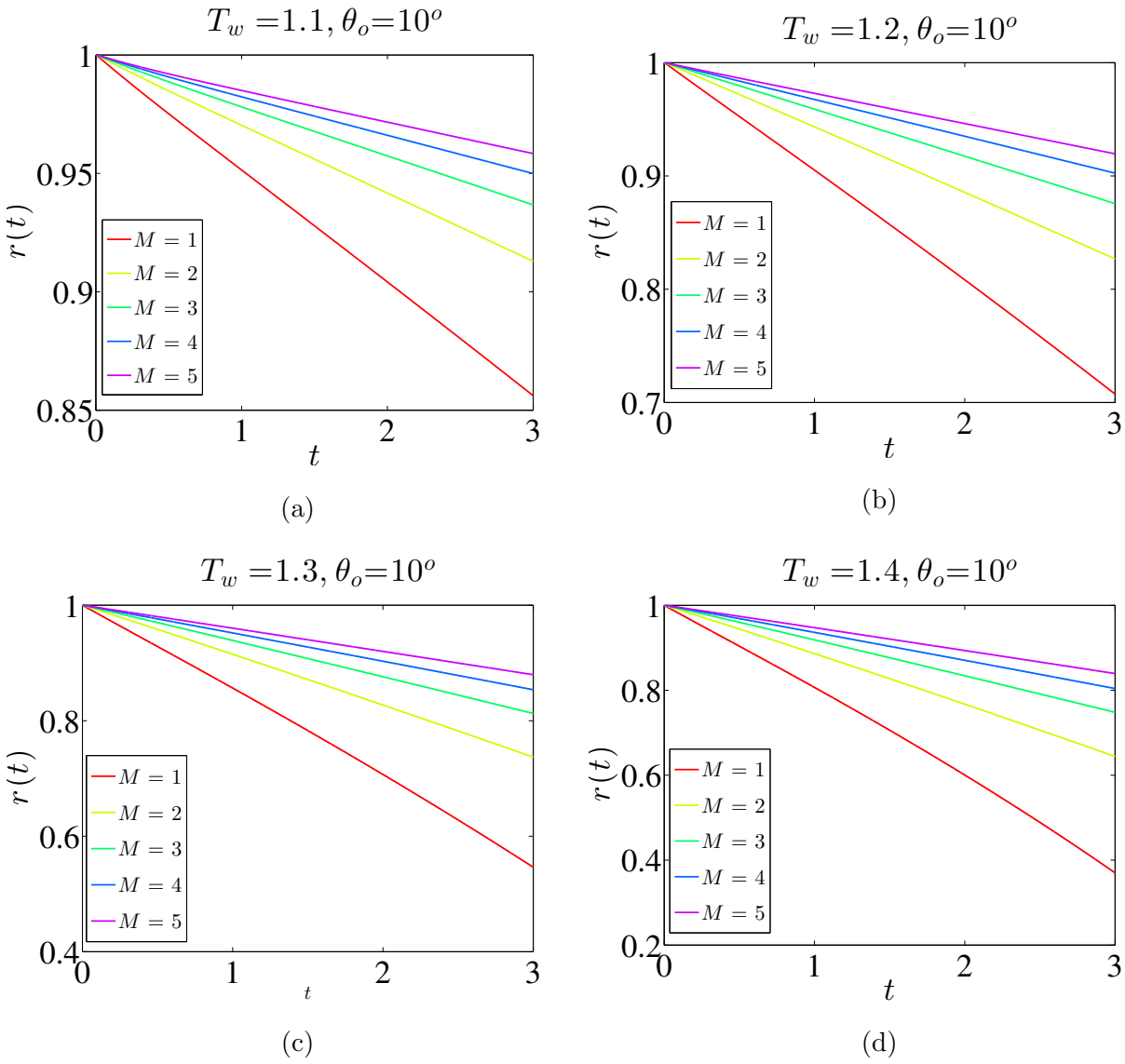

Figure 4.16: Results of values of wetted radius $r(t)$ vs time t for (a) $T_w = 1.1$, (b) $T_w = 1.2$, (c) $T_w = 1.3$, and, (d) $T_w = 1.4$, for different values of M and $\theta_o = 10^o$.

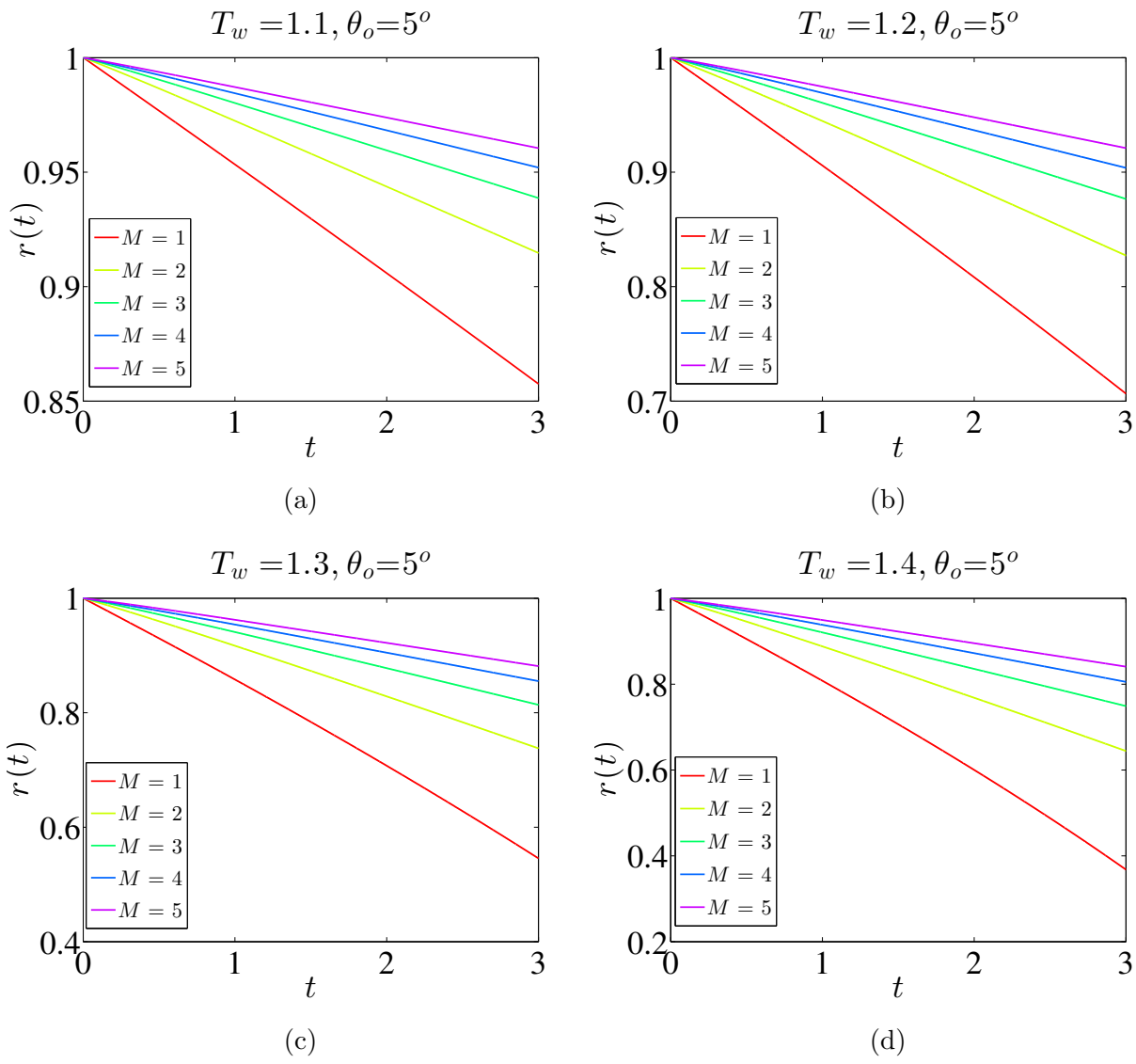

Figure 4.17: Results of values of wetted radius $r(t)$ vs time t for (a) $T_w = 1.1$, (b) $T_w = 1.2$, (c) $T_w = 1.3$, and, (d) $T_w = 1.4$, for different values of M and $\theta_o = 5^o$.

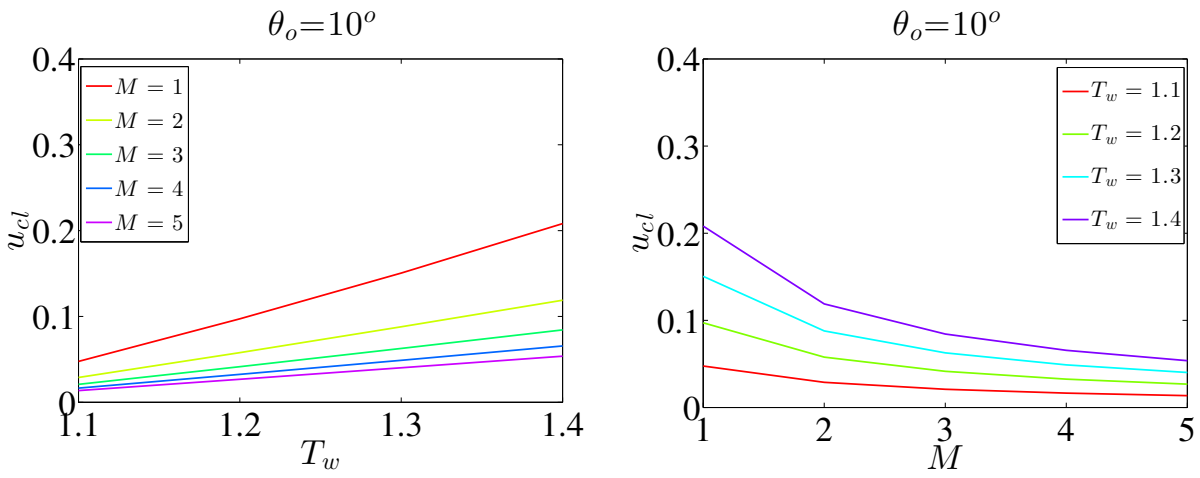

(a) (b)

Figure 4.18: Results of contact line speed u_{cl} (a) vs T_w for different values of M and, (b) vs M for different values of T_w.

Chapter 5

EVAPORATION OF DROPLET ON PERIODIC SOLID SUBSTRATES

In this Chapter, the evolution equation

$$h_t = -\frac{1}{3}\frac{\partial}{\partial x}\left((h+s)_{xxx}h^3\right) - \frac{T_w - 1}{M+h}, \tag{5.1}$$

is solved for the case in which the solid-liquid interface is periodic. We consider a single-mode harmonic solid as the simplest case of a periodic substrate. As shown in Figure 5.1, the solid-liquid interface $s(x)$ is taken be a single-mode sinusoidal function. In view of the assumption that the first $s_x(0)$ and third derivatives $s_{xxx}(0)$ of the height of solid-liquid interface vanish at the location of symmetry line, $x = 0$, the droplet symmetry line must meet the solid-liquid interface at either a peak or a trough. Since we do not expect fundamentally different behaviors between these cases, only the latter configuration is considered in this work: the droplet center is chosen to be over a trough. Accordingly, the height $s(x)$ of the solid-liquid interface is described by

$$s(x) = -a\cos(kx), \tag{5.2}$$

where a, and k respectively denote the amplitude and the wave number, i.e. $k = 2\pi/\lambda$. As shown in Figure 5.1, $r(t)$, θ, and α respectively denote the wetted radius, the contact angle, and the apparent contact angle i.e. the angle between the horizon and the tangent line to the liquid-vapor interface at the contact line. We represent the vertical distance between the interface and the horizon at the contact line by an intermediate variable $h^f(x,t)$. Accordingly, $\alpha(t)$ and θ are respectively defined by the slopes h^f_x and $h^f_x - s_x$ at $x = r(t)$. At any instance, $h^f(x,t)$ and the droplet thickness $h(x,t)$ are geometrically related as follows:

$$h(x,t) = h^f(x,t) + s(r(t)) - s(x). \tag{5.3}$$

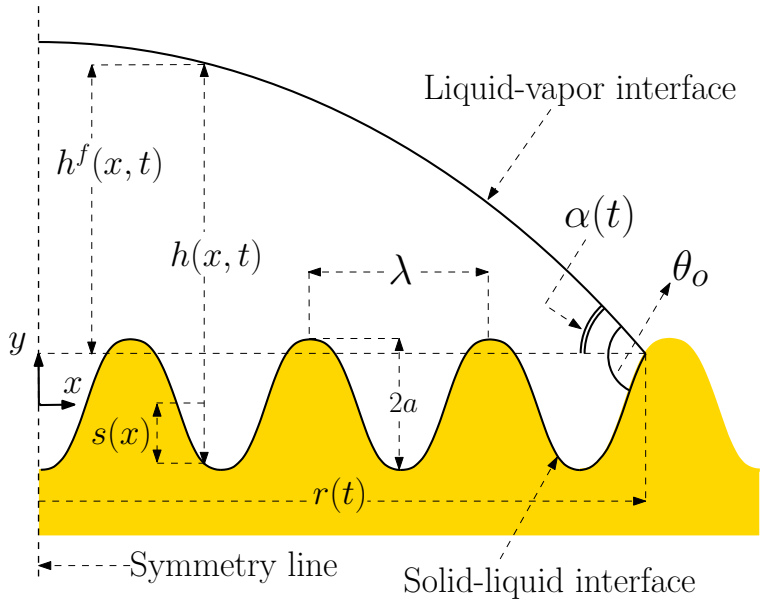

Figure 5.1: 2D Schematic of a symmetric liquid drop on a periodic solid substrate.

The first derivative of (5.3) with respect to x at $r(t)$ implies that $\alpha(t)$ and θ may be determined, respectively, by the slopes $h_x + s_x$ and h_x at the contact line. Hence, although defining h^f is essential to understand the geometry, the problem may be analyzed without its direct use.

As a result of choosing $h^f(0,0)$ and $r(0)$ as L_x and L_y the length scales in x and y directions, the solid-liquid interface in dimensionless form is

$$s(x) = -\Gamma_1 \cos(2\pi\Gamma_2 x), \tag{5.4}$$

where Γ_1 and Γ_2 are dimensionless numbers defined as

$$\Gamma_1 = \frac{a}{h^f(0,0)}, \qquad \text{and,} \qquad \Gamma_2 = \frac{r(0)}{\lambda} = \frac{r(0)k}{2\pi} \tag{5.5}$$

As mentioned in Chapter 2 in order to satisfy the lubrication approximation, scale L_y of the transverse variation needs to be much smaller than its lateral counterpart L_x, so that the aspect ratio ϵ defined in (2.34) obeys $\epsilon \ll 1$. To ensure that the solid-liquid interface also

follows the lubrication approximation, a dimensionless number ξ defined as

$$\xi = \frac{a}{\lambda} = \frac{ak}{2\pi}, \tag{5.6}$$

which characterizes the slope of solid-liquid interface, must also obey $\xi \ll 1$. Note that one of the three dimensionless numbers Γ_1, Γ_2 and ξ is dependent on the other two and thus, assigning values to any two of them, is sufficient to fully describe the substrate. These three are related to each other via following equation,

$$\xi = \epsilon\Gamma_1\Gamma_2, \tag{5.7}$$

where, ϵ is fixed once the initial value of the contact angle $\theta(0)$ is chosen.

In this Chapter, the evolution equation (5.1) is solved, separately for pinned and moving contact lines on periodic substrates with the dimensionless parameters T_w, M and $\theta(0)$ chosen as

$$T_w = 1.2, \qquad M = 2, \qquad \text{and} \qquad \theta(0) = 5^o.$$

For the case of pinned contact line solutions are provided for fixed value of Γ_2 and different values of ξ but for the case of moving contact line, where the results become more interesting, we solve the problem for single-mode periodic substrates with different values of ξ and Γ_2. We then create more complex substrate profiles by adding more modes, including quasi-periodic waveforms, and compare the results with the simpler cases.

5.1 *Evaporation of droplets on single-mode periodic solid substrates for the case of pinned contact line*

For the case in which the contact line is pinned i.e. $r(t) = 1$, the evolution equation (5.1) is numerically solved subject to circular cap initial condition and based on the symmetry conditions and contact line conditions, respectively, presented below

$$\left.\begin{array}{c} h^f_{xxx}(x,0) = 0 \\ h_x(0,t) = 0, \text{ and, } h_{xxx}(0,t) = 0, \\ h(1,t) = 0, \text{ and, } h_{xx}(1,t) + s_{xx}(1) = 0. \end{array}\right\}$$

The quantities of interest for this case are the droplet thickness $h(x,t)$, evaporative mass flux $J(x,t)$ and contact angle $\theta(t)$ which are shown over time for a reference case of $\xi = 0.003$ in Figures 5.2-5.4.

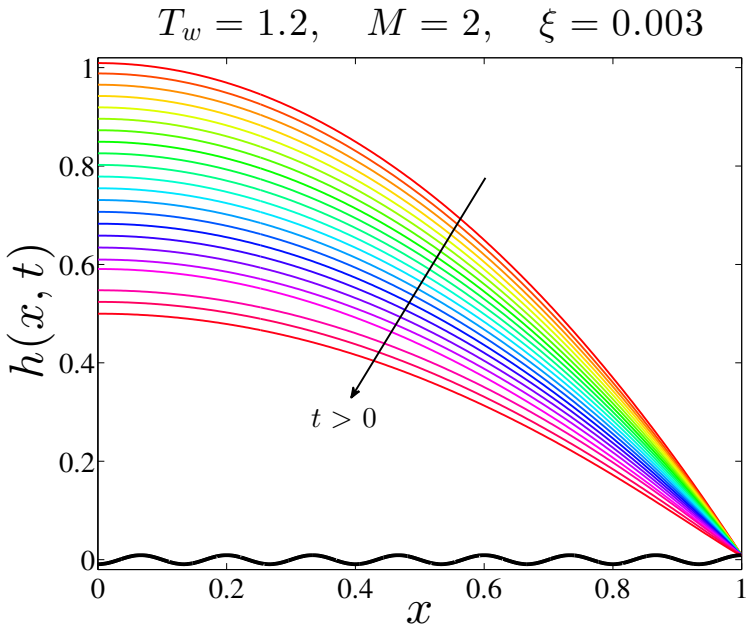

Figure 5.2: Droplet profile while evaporating in pinned contact line mode on the harmonic solid substrate with $\xi = 0.003$ and $\Gamma_2 = 7.5$.

Similar to the case of flat substrate, both the thickness $h(0,t)$ of the droplet at the symmetry node and the contact angle $\theta(t)$ are decreasing in time while the contact line is pinned. Also, the maximum of evaporative mass flux J is always located at the contact line while $J(x,t)$ is increasing everywhere over time (except at the contact line location where h is minimum and thus the value of J is maximum and constant). Numerical results for $h(x,t)$ and $J(x,t)$ have been produced for different values of ξ indicating that for all values of ξ the droplet profile and evaporation mass flux $J(x,t)$ are qualitatively analogous to Figures 5.2 and 5.3. Due to this similarity these results will not be shown.

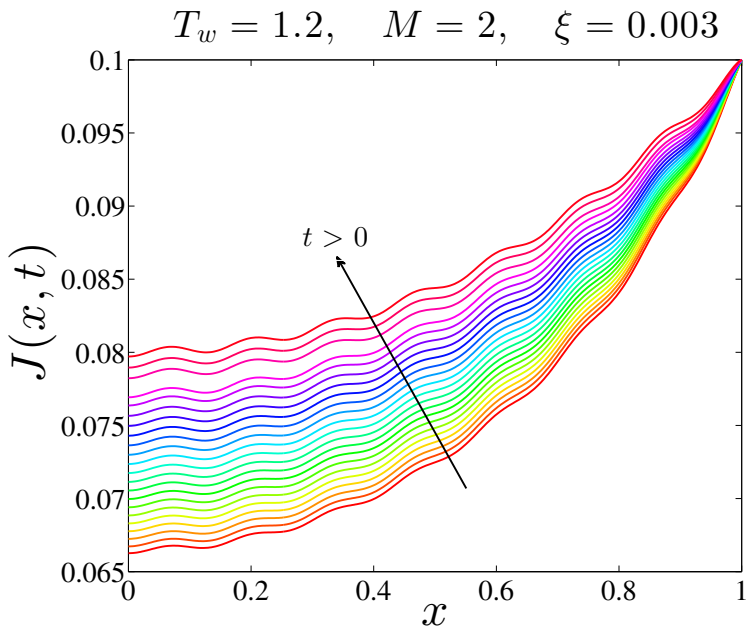

Figure 5.3: Results of evaporative mass flux $J(x,t)$ as the droplet evaporates in pinned contact line mode on the harmonic solid substrate with $\xi = 0.003$ and $\Gamma_2 = 7.5$.

Similar to the results for the flat case, Figure 5.4 shows that the contact angle decreases almost linearly for a range of time until the critical time t_{cr}, the time at which the local contact angle goes to zero. Near the t_{cr} the dynamics becomes much faster and thus, the value of contact angle starts to drop much more rapidly. Note that, similar to the flat case, we observed the mesh-dependency issue in producing $\theta(t)$ for the periodic case and treated

it using the same method explained in section 4.1.

Figure 5.5 reveals that the contact angle follows a similar behavior for different values of ξ, while with increasing ξ the value of t_{cr} increases. Since the contact line is pinned on a peak, with increasing ξ the amount of liquid mass available near the contact point increases. Thus, for larger values of ξ the thermal resistance becomes larger and therefore the evaporation occurs at a slower pace and t_{cr} increases.

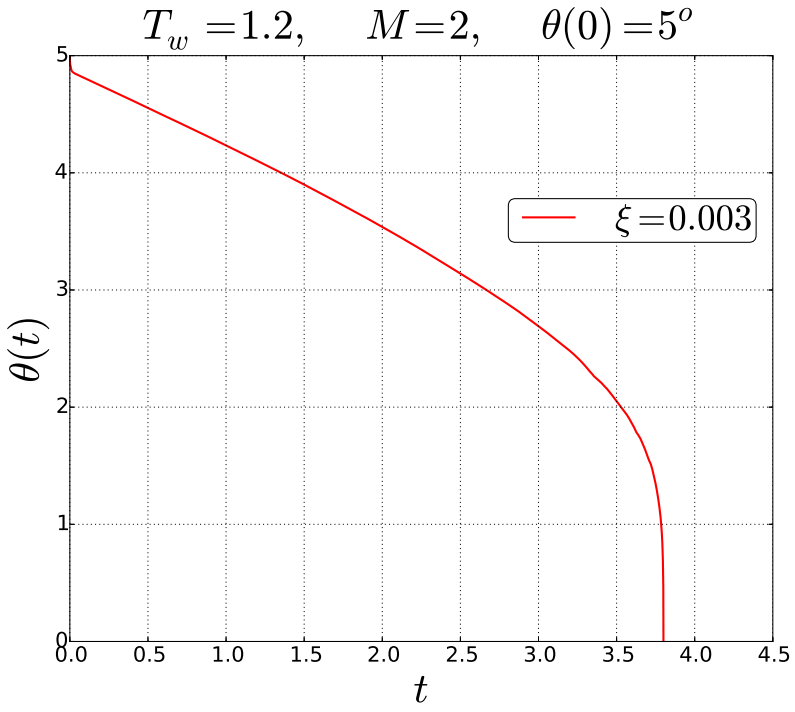

Figure 5.4: Results of contact angle $\theta(t)$ as the droplet evaporates in pinned contact line mode on the harmonic solid substrate with $\xi = 0.003$ and $\Gamma_2 = 7.5$.

In conclusion, for the case of pinned contact line on single mode harmonic substrate, the dynamics are very similar to what occurs on a flat surface except that the thermal resistance depends on the local thickness, leading to an oscillatory component to the flux, and also that as the slope ratio of the substrate increases it takes more time to reach to the critical time t_{cr}.

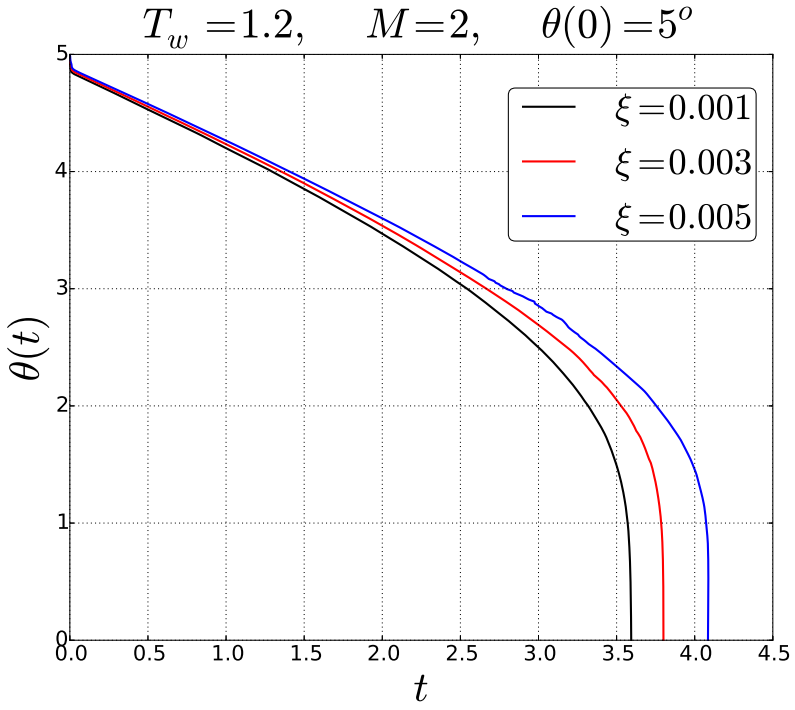

Figure 5.5: Results of contact angle $\theta(t)$ for the case of pinned contact line on the harmonic solid substrate with $\Gamma_2 = 7.5$ and different values of ξ.

5.2 Evaporation of droplets on periodic solid substrates for the case of moving contact line

For the case in which the contact line is moving and the contact angle is fixed, i.e. $\theta(t) = \theta(0) = \theta_o$, the evolution equation (5.1) is numerically solved for the circular cap initial condition and based on the symmetry conditions and contact line conditions, respectively, presented below

$$\left.\begin{array}{c} h^f_{xxx}(x,0) = 0 \\ h_x(0,t) = 0, \text{ and, } h_{xxx}(0,t) = 0, \\ h(r(t),t) = 0,, \; h_{xx}(r(t),t) + s_{xx}(r(t)) = 0, \text{ and, } h_x(r(t),t) = \Theta_o. \end{array}\right\}$$

Similar to the case of moving contact line on a flat substrate, the interesting quantities in this case are the droplet thickness $h(x,t)$, evaporative mass flux $J(x,t)$, wetted radius $r(t)$, and the contact line speed $u_{cl}(t)$. But in addition, we study the evolution of the apparent contact angle $\alpha(t)$, i.e. the contact angle that the liquid appears to make with the solid surface when viewed at such coarse resolution that the substrate appears flat. $h(x,t)$ and $r(t)$ are determined simultaneously as a result of solving the evolution equation. Once $h(x,t)$ and $r(t)$ are known $J(x,t)$, $u_{cl}(t)$ and $\alpha(t)$ are computed as secondary quantities. We analyze the problem for (i) single-mode periodic, (ii) two-mode periodic, and (iii) multi-mode quasi-periodic substrates.

5.2.1 Single-mode periodic substrates

As a reference case, we take a droplet that initially covers 10.5 wavelengths of the solid on each side of the symmetry line (i.e. $\Gamma_2 = 10.5$), a prescribed contact angle $\theta_o = 5^o$, and a solid slope ratio $\xi = 0.006$. Such a configuration has $\epsilon = 0.0437$ and $A = 0.0131$. Figures 5.6-5.8 show the droplet profile, evaporative mass flux and wetted radius over 10.5 units of dimensionless time, for this reference case.

Figure 5.6 illustrates the droplet shape evolution for the reference case. As anticipated, the droplet thickness decreases on average; however, due to the global effect of the contact line motion over peaks and troughs, h shows non-monotonic variation near the centerline. Since the droplet adapts its shape to the local slope of the solid such that the contact angle remains fixed, the droplet profile varies from its initial shape and thus simpler models, which *assume* that the droplet cross section remains circular along the evaporation, are not valid. For the reference case presented, the mean square error of the departure of the profile from a static shape is on the order of 5%.

Results for $J(x,t)$ are presented in Figure 5.7. Consistent with equation (2.61), the evaporative flux increases similar to the flat case: its maximum is located at the contact line and the maximum value is constant over time. However, on a periodic substrate, (i) J is oscillatory

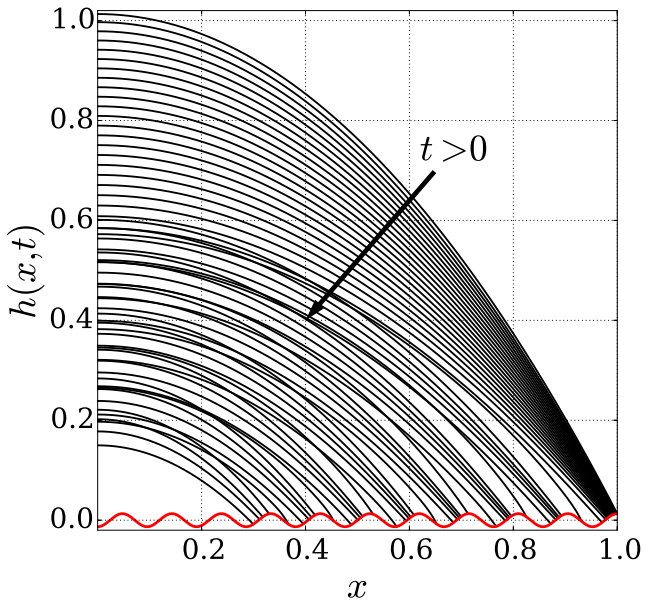

Figure 5.6: Droplet profile while evaporating on the single-mode periodic solid substrate, for the reference case. (Profiles are plotted over equal time increments.)

along the x-axis since the substrate is sinusoidal and (ii) some minor temporal variation is observed near the centerline as a consequence of the discussed temporal variation in h.

The wetted radius $r(t)$ is plotted for both the reference case and the corresponding flat substrate in Figure 5.8. In contrast with what we found for the flat case, $r(t)$ exhibits a periodic time variation superposed on a linear decrease, indicating that the speed u_{cl} of the contact line in the x direction is no longer constant. Figure 5.8 also shows that the slope of a linear fit to $r(t)$ (neglecting the initial transient), i.e. the average velocity $\bar{u}$ of the contact line, is approximately 25% larger than the constant contact line speed u_f observed for the flat case. Interestingly, for all the cases we studied, we found that $\bar{u}$ is larger than u_f and that while it is only weakly dependent on Γ_2, it increases with increasing slope ratio ξ. The fact that $\bar{u} \neq u_f$ is consistent with the nonlinearity of the problem, but to investigate why nonlinearities lead to faster average evaporation, further analysis is required regarding the contact line motion.

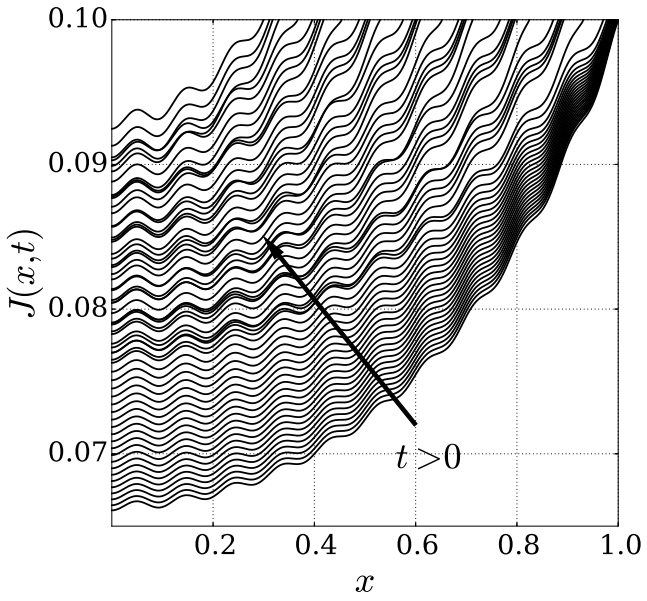

Figure 5.7: The evaporative mass flux of an evaporating droplet on the single-mode periodic solid substrate, for the reference case.

To relate the dynamics of the contact line to the solid profile, the (negative) values of u_{cl} are plotted as a function of $r(t)$ and presented in Figure 5.9. The red and blue dashed lines represent the location of peaks and troughs respectively, so that at any instant, one can identify the contact line speed and position, simultaneously. Focusing on one cycle (shown in dark in Figure 5.9), the contact line slows from the peak to the first inflection point; it accelerates between the first and second inflection points such that its maximum is achieved near the second, after which it slows down until it reaches the second peak. The contact line dynamics during the subsequent periods is similar, except that both the maximum speed of contact line and the speed at which it moves over the peaks decrease. To analyze this behavior, each term at the right hand side of the evolution equation was evaluated and monitored separately over time. The results indicate that the capillary flux term dominates the evaporative flux near the contact line and therefore the motion is governed mainly by the shape of the solid. At any time, the distance required for the contact line to move such

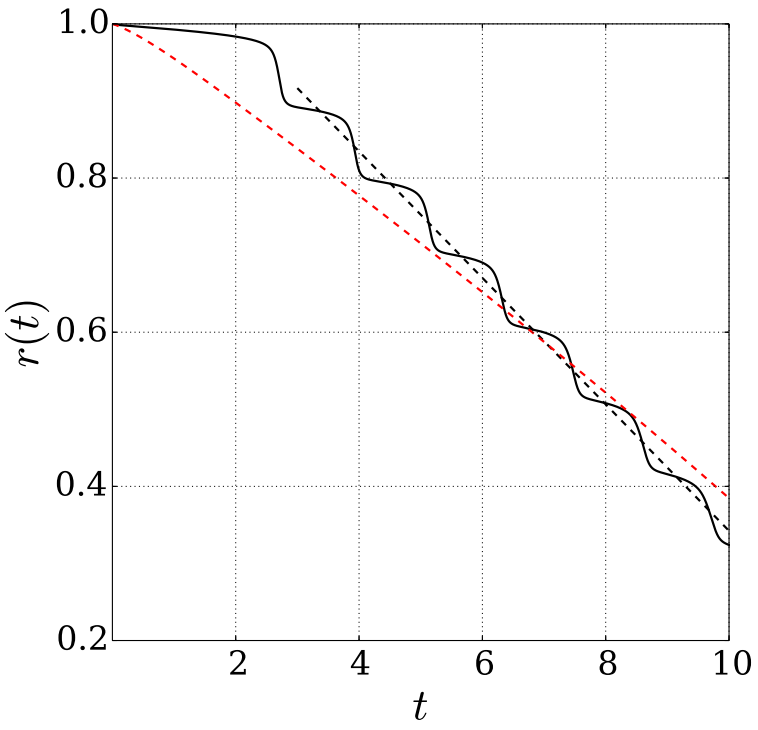

Figure 5.8: The wetted radius $r(t)$ on the single-mode periodic solid substrate, for the reference case. The black dashed line represent the fitted line to $r(t)$, neglecting the initial transient, and the red dashed line represents the results for the flat case. The slopes of the black and red dashed lines are 0.081 and 0.065, respectively.

that the specified contact angle is maintained, and consequently the instantaneous speed of the contact line, are highly dependent on the substrate profile. As shown in Figure 5.9, the contact line loses speed where the solid curvature is negative and gains speed otherwise. Rather than plotting the contact line speed as a function of location (Figure 5.9), it is plotted as a function of time in Figure 5.10. As seen, for each period of the solid, the motion may be divided into a low-speed phase, in which $u_{cl} < u_f$, and a high-speed phase which includes a spike. The dashed box, which zooms in one of these low-speed and high-speed regions, indicates that (i) during a low-speed period the speed is near zero and (ii) the duration of a low-speed region is relatively long. Accordingly, one who monitors the location of the contact

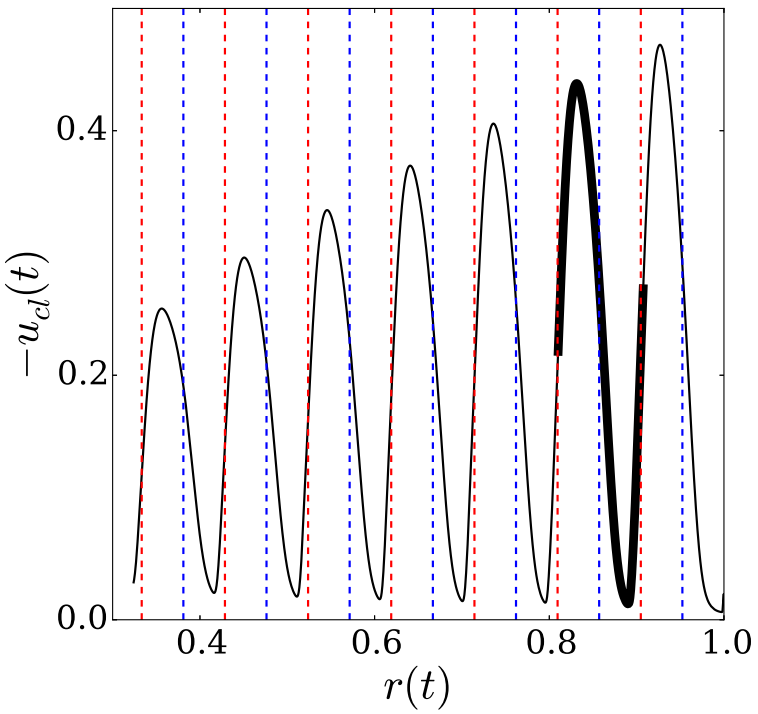

Figure 5.9: The contact line speed u as a function of the wetted radius $r(t)$, for the reference case. The red and blue dashed lines represent the location of peaks and troughs, respectively. The thick region is corresponding to the motion over the second period of the solid.

line with limited accuracy might assume that it is pinned for a range of time mimicking a step-like motion. Thus, a step-like motion is captured by our lubrication model. This step-like motion is qualitatively similar to the experimentally observed "stick-slip behavior" of the contact line and is consistent with the "apparent stick-slip" behavior described by Espin and Kumar [9] and Savva and Kalliadasis [19], discussed in the Introduction.

Figure 5.10 also shows that as the contact line recedes towards the center-line, its maximum speed decreases while the width of the high-speed regions increases i.e. for the wave-lengths that are further from the center-line, the maximum speed of the contact line is larger and the width associated with the high-speed region is smaller. Our results show that this process happens in such way that the time t_λ that it takes for the contact line to travel one wave-

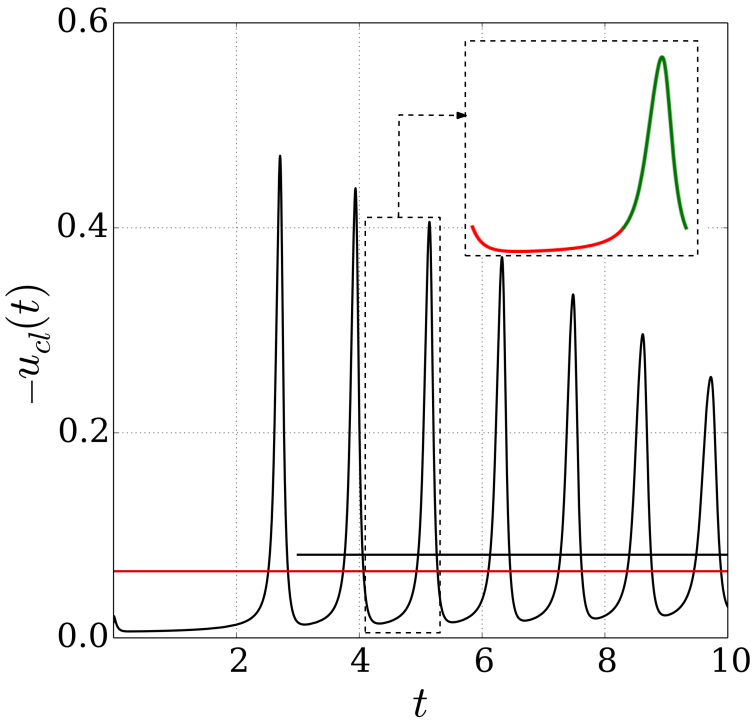

Figure 5.10: $u_{cl}(t)$ on the periodic solid substrate, for the reference case. The dashed box represents the results for one low speed region shown with red color followed by a high speed spike illustrated in green. The black horizontal line represent the average speed $\bar{u}$, neglecting the initial transition. The red line denotes u_f, the speed for the flat case. For the data presented $\bar{u}$ and u_f are equal to 0.081 and 0.065, respectively.

length of the substrate is approximately constant over time and independent of how far the corresponding wave-length is from the center-line. This is best illustrated by figure 5.11a which shows the value of the apparent contact angle $\alpha(t)$ as a function of time. Recall that $\alpha(t)$ adjusts its value to the local slope of the solid, $s_x(r(t))$, such that the contact angle remains constant. As a result, the points at which $\alpha = \theta_o$ correspond to peaks (shown with cyan circles) and troughs, and the points at which α reaches to its maximum or minimum values correspond to the inflection points of the solid profile. Except for an initial transient, the distance between two adjacent cyan circles is constant over the entire process, meaning

that the time t_λ that it takes for the contact line to move from one peak to another is constant, i.e. $\alpha(t)$ is a periodic function. As mentioned above, this may be discovered from plots like those in Figure 5.8 and 5.10, but focusing on $\alpha(t)$ allows a convenient analysis of the dynamics by Fourier decomposition.

Figure 5.11b shows the power spectrum of $\alpha(t)$ in blue. We see that all the major peaks are located at the frequencies that are harmonics of a single primary frequency $f_p = 1/t_\lambda$. As mentioned earlier, the contribution of these harmonics to the mean speed is such that the nonlinearity of the solid leads to faster evaporation. As expected, we found that once the linear signal is subtracted from $r(t)$, the peaks in power spectrum of the resulting values are also located exactly at harmonics of $f_p = 1/t_\lambda$. This is illustrated with red-dashed lines in Figure 5.11b.

We generated similar results for different values of ξ and Γ_2 and found that while f_p increases with increasing Γ_2 and ξ, illustrated in Figures 5.12 and 5.13, the behavior of the contact line is qualitatively similar for all cases. Therefore, we conclude that for any given single-mode periodic substrate, the time t_λ that it takes for the contact line to travel one wavelength is independent of how far the corresponding wavelength is from the centerline, i.e. $\alpha(t)$ is a periodic function. Such a conclusion may be validated by showing that the total average speed $\bar{u}$ is equal to the average speed for each wavelength λ/t_λ. This equality is found to be satisfied for all cases we studied, including the presented case for which $\bar{u} = 0.081$ and $\lambda/t_\lambda = 0.08$.

In summary, for contact line motion on a single-mode periodic substrate, we found that (i) the "apparent stick-slip" behavior is captured by our lubrication model; (ii) the nonlinearity of the problem leads to faster evaporation such that the average speed $\bar{u}$ of the contact line is larger than the constant speed u_f observed for the flat case; (iii) the apparent contact angle $\alpha(t)$ is periodic, i.e. the average speed λ/t_λ for each period is constant over different wavelengths and therefore is the same as the global average speed $\bar{u}$; and (iv) as expected of a nonlinear system with periodic coefficients, the power spectrum of α shows a typical "single-mode with harmonics" behavior.

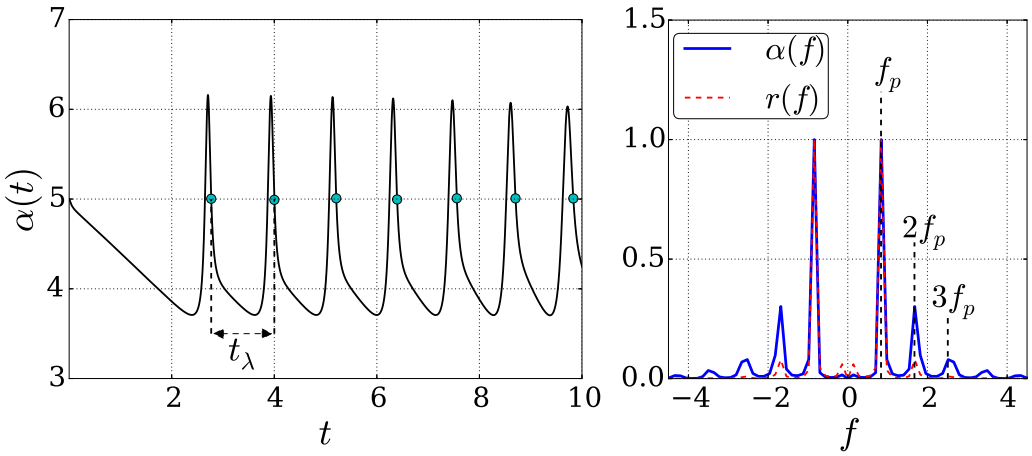

Figure 5.11: The apparent contact angle α on a single-mode periodic substrate, for the reference case. (a): α as a function of time. The circles in cyan represent the time at which the contact line is located on a peak; The distance between each two adjacent circle denotes the time t_λ that it takes for the contact line to move over one wavelength of the solid. (b): Normalized power spectrum of $\alpha(t)$ (shown in blue) and $r(t)$ (shown in red), neglecting the initial transient. All the major peaks are located at harmonics of $f_p = 0.84$ indicating that $t_\lambda = 1.19$.

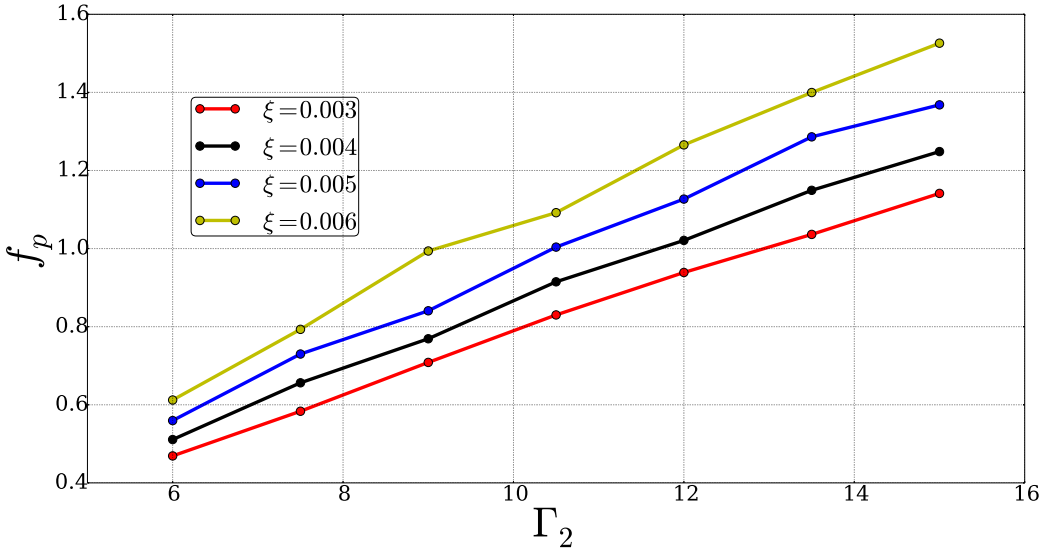

Figure 5.12: Results of primary frequency f_p vs. Γ_2 for given values of ξ.

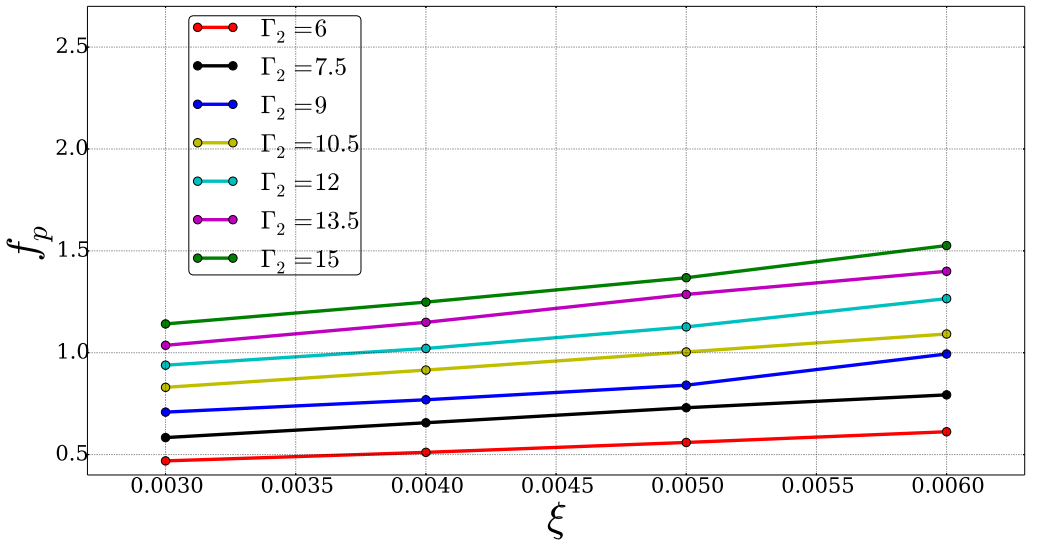

Figure 5.13: Results of primary frequency f_p vs. ξ for given values of Γ_2.

5.2.2 Two-mode periodic substrates

Having established what happens in the simplest case of a periodic substrate, the question is: what happens with a more complex substrate variation? One way to approach this question is to build up complexity by adding more modes. We generated a two-mode periodic substrate $s_2(x)$ by a linear combination of a high-frequency $s_H(x)$ and a low-frequency $s_L(x)$ harmonic function, i.e.

$$s_2(x) = -\frac{1}{2}\left(\overbrace{a_H \cos(k_H x + \phi_H)}^{-s_H(x)} + \overbrace{a_L \cos(k_L x + \phi_L)}^{-s_L(x)}\right). \tag{5.8}$$

To ensure that the droplet center is over a trough, we choose $\phi_H = \phi_L = 0$, for simplicity we take $a_H = a_L = a$, and to scale the problem in x and y directions we choose $r(0)$ and $h^f(0,0)$. As a result, the dimensionless form of $s_2(x)$ is

$$s_2(x) = -\sum_{i=1}^{2} \frac{\Gamma_1}{2} \cos(2\pi\Gamma_2\Omega_i x), \tag{5.9}$$

where

$$\Gamma_1 = \frac{a}{h^f(0,0)}, \quad \Gamma_2 = \frac{r(0)}{\lambda_L}, \quad \Omega_1 = \frac{k_H}{k_L}, \quad \text{and} \quad \Omega_2 = 1, \tag{5.10}$$

where λ_L is the wavelength corresponding to s_L. The slope of s_2 is bounded by a dimensionless number ξ_2, defined as

$$\xi_2 = a(k_H + k_L), \tag{5.11}$$

and hence $\xi_2 \ll 1$ serves as a sufficient condition for the lubrication approximation to be valid. This slope ratio is dependent on the the other dimensionless numbers via

$$\xi_2 = \epsilon A\Gamma \sum_{i=1}^{2} \Omega_i. \tag{5.12}$$

Thus, assigning values to Ω_1, Γ_1, and Γ_2 and choosing a contact angle θ_o is sufficient to describe the problem.

As a reference case, a two-mode substrate s_2 with $\Omega_1 = 3$, $\Gamma_1 = 0.0076$, and $\Gamma_2 = 4.5$ and a droplet with contact angle $\theta_o = 5^o$ were considered. Figure 5.14 shows the two-mode substrate together with its corresponding single modes for the sample case of $\Omega_1 = 3$. In

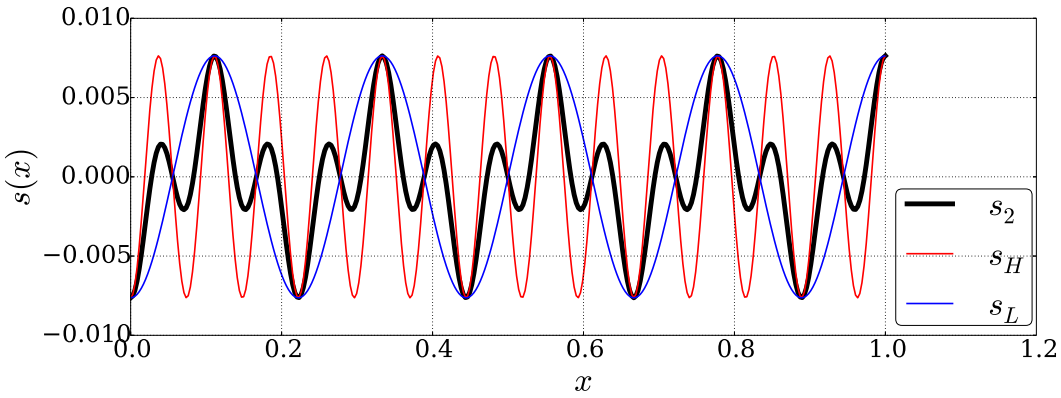

Figure 5.14: The two-mode substrate s_2 together with its corresponding high-frequency and low-frequency single modes s_H and s_L for the case of $\Omega_1 = 3$, $\Gamma_1 = 0.0076$ and $\Gamma_2 = 4.5$.

order to probe nonlinearities and to test for superposition, the problem is solved for s_2, s_L, and s_H, separately. For each substrate, the numerical solution is achieved over 10.5 units of dimensionless time which is enough for the contact line to move over three wavelengths on s_2 and s_L and nine wavelengths on s_H.

The black line in Figure 5.15a gives the apparent contact angle $\alpha_2(t)$ for evaporation on s_2. As shown, $\alpha_2(t)$ is a more complex waveform compared to the single-mode case but is still periodic. One may interpret $\alpha_2(t)$ as a periodic waveform with "fundamental" frequency f_{p_2} that is modulated by a subharmonic carrier signal of frequency $f_{p_2}/3$. Figure 5.15b quantitatively confirms such an interpretation by showing that all the peaks of the power spectrum are located at the frequencies that are either sub-or-super-harmonics of a single primary frequency f_{p_2}. As a result, the time t_{λ_2} that it takes for the contact line to move over one wavelength of s_2 is constant during the evaporation. Accordingly, similar to what we found for the single-mode substrate, the average speed λ_2/t_{λ_2} of each period is the same for all wavelengths of s_2 and is equal to the global average speed $\bar{u}_2$. (Note that $\lambda_2 = 2\pi/\Gamma_2$ and for this case $t_{\lambda_2} = 3/f_{p_2}$.)

We found that a linear superposition of the results for single modes fails to predict the solution

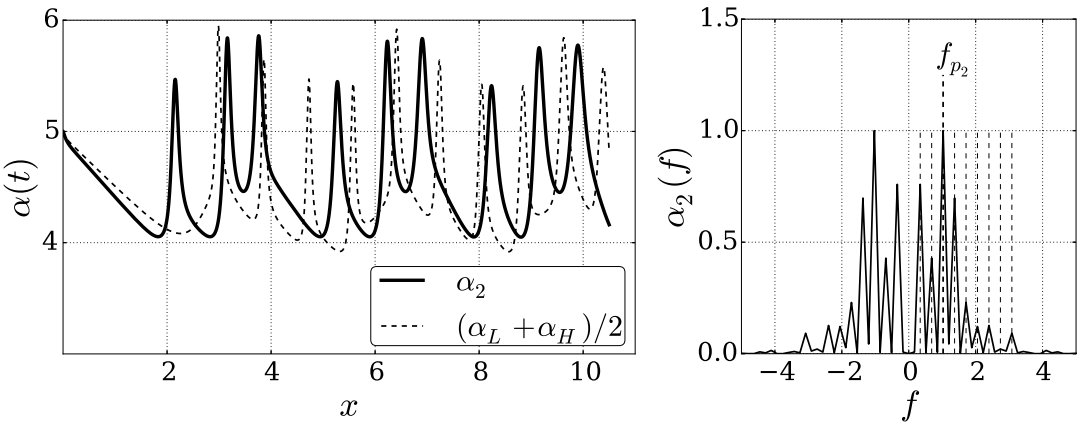

Figure 5.15: The apparent contact angle as the droplet evaporates on the two-mode periodic solid substrate, for the reference case. (a): α_2 as a function of time. The dashed line represents the average of α_L and α_H which respectively are the contact angle produced as a result of separately solving the problem on s_L and s_H. (b): Normalized power spectrum of $\alpha_2(t)$, neglecting the initial transient. All the major peaks are located at either harmonics or subharmonics of f_p. The primary frequencies for this case are $f_{p_2} = 1.0272$, $f_{p_H} = 1.207$, and $f_{p_L} = 0.229$.

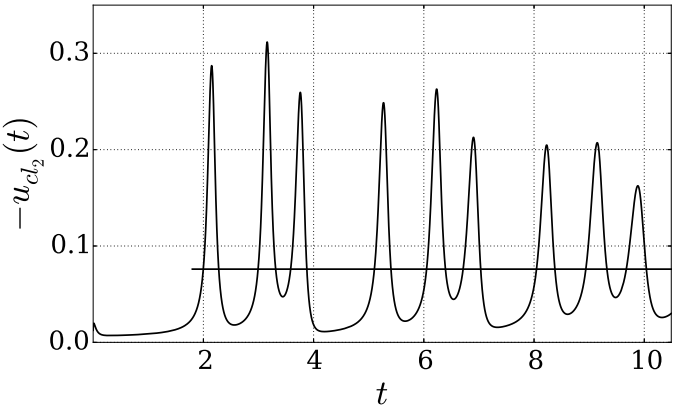

Figure 5.16: The contact line speed $u_{cl_2}(t)$ as the droplet evaporates on the two-mode periodic solid substrate, for the reference case. The horizontal line represents the global average speed $\bar{u}_2$, neglecting the initial transient. For the data presented $\bar{u}_2 = 0.0760$.

on s_2; this is expected since the problem is nonlinear. Figure 5.15a confirms this by showing the disparity between the average solution $(\alpha_L + \alpha_H)/2$ and the two-mode solution α_2. Additionally, we investigated the dependence of the primary frequency f_{p_2} of the two-mode substrate on the single mode frequencies f_{p_H} and f_{p_L} and thus calculated each separately. Interestingly, we found that regular sums and differences of f_{p_H} and f_{p_L} or simple relations involving Ω_1 fail to predict f_{p_2} and thus we conclude that the problem exhibits a phase-locking behavior for this case.

The (negative) values of the contact line speed u_{cl_2} are presented in Figure 5.16. As seen, the results are more complex than the those for the single-mode substrates, but follow the same overall apparent stick-slip behavior: the maxima decrease while the width of the high-speed regions increase such that the global average speed $\bar{u}_2$ is the same as the average speed $\lambda_2 f_{p_2}/3$ for each period. This is verified for the reference case since the average speed $\bar{u}_2$, shown with the horizontal line in Figure 5.16, is in good agreement with $\lambda_2 f_{p_2}/3$.

We generated many two-mode periodic substrates with different rational values of Ω_1 and solved the problem separately for the two-mode substrate and each of its corresponding single-mode profiles. We found that (i) similar to the single-mode profiles, the contact line exhibits an apparent stick-slip behavior; (ii) the apparent contact angle is still periodic but the peaks of its power spectrum are located at the subharmonics and harmonics of a single primary frequency f_{p_2}; (iii) the overall evaporation is faster compared to the flat case; (iv) due to the strong nonlinearity of the problem, the solution on two-mode substrates may not be obtained by the linear superposition of the single-mode results; and (v) sums and differences of single-mode frequencies f_{p_L} and f_{p_H} fail to produce the primary frequency f_{p_2} of the two-mode case and there is no simple relation between f_{p_2} and f_{p_L} and f_{p_H} that holds for all values of Ω_1. We conclude that the interesting phase-locking behavior is a general result over the range of parameters studied.

5.2.3 Multi-mode quasi-periodic substrates

Our model is not limited to the periodic substrates and is therefore capable of solving the problem for any 2D symmetric solid profile. Hence we studied shapes that are closer to a random configuration. The number of modes was increased to add complexity and irrational values were assigned to the wavelength ratios Ω_i to create quasi-periodic shapes. Here we consider the reference case in which, three modes are combined as follows

$$s_3(x) = -\sum_{i=1}^{3} \frac{\Gamma_1}{3} \cos(2\pi\Gamma_2\Omega_i x), \tag{5.13}$$

with the wavelength ratios chosen as

$$\Omega_1 = \frac{2\pi}{3}, \quad \Omega_2 = \sqrt{\pi}, \quad \text{and} \quad \Omega_3 = 1, \tag{5.14}$$

$\Gamma_2 \approx 1.85$ and $\Gamma_1 = 0.0024$. Figure 5.17 shows the corresponding quasi-periodic solid-liquid interface, which is no longer periodic and appears fairly random.

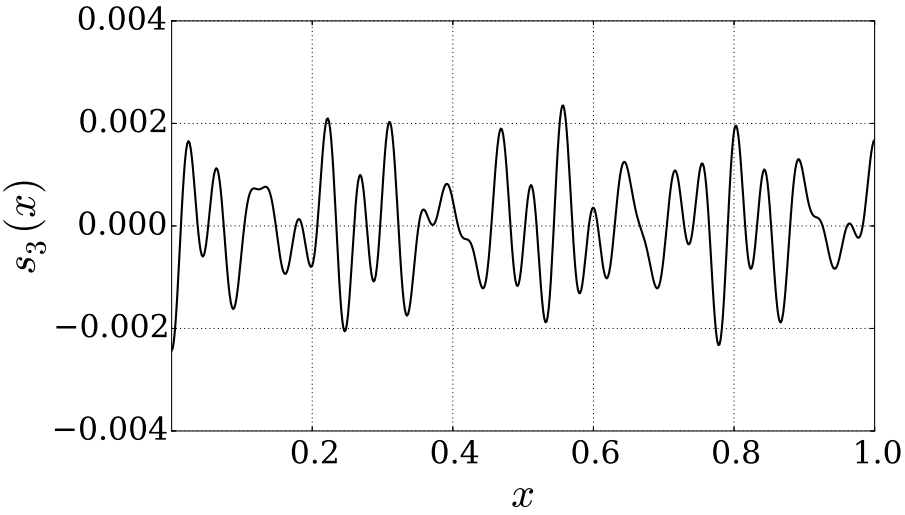

Figure 5.17: Three-mode substrate produced by irrational wavelength ratios $\Omega_1 = 2\pi/3, \Omega_2 = \sqrt{\pi}$, and $\Omega_3 = 1$.

The problem is solved numerically with contact angle $\theta_o = 5^o$. The apparent contact angle $\alpha_3(t)$ and its power spectrum $\alpha_3(f)$ are shown in Figure 5.18a and 5.18b, respectively.

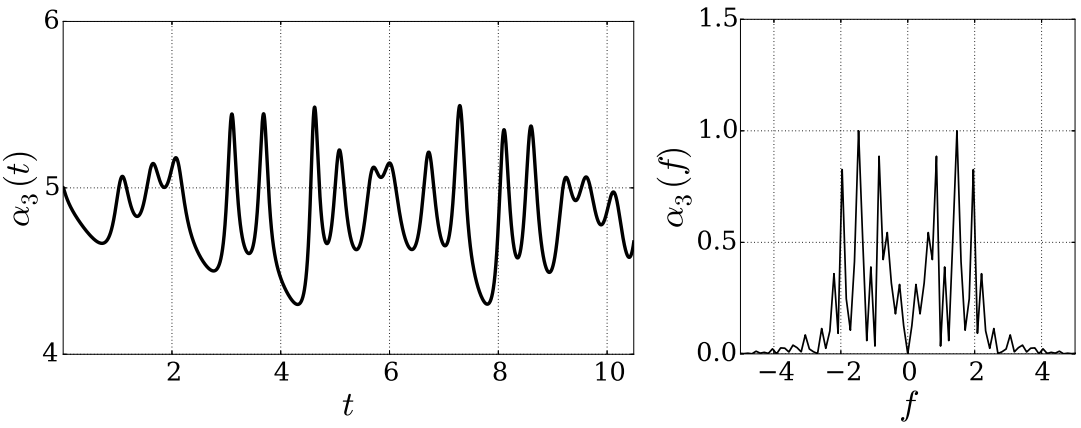

Figure 5.18: Results for three-mode substrate produced by irrational wavelength ratios $\Omega_1 = 2\pi/3, \Omega_2 = \sqrt{\pi}$, and $\Omega_3 = 1$ and the specified contact angle $\theta_o = 5^o$. (a): the apparent contact angle α_3 over time. (b): Normalized power spectrum of $\alpha_2(t)$, neglecting the initial transient. In contrast with periodic substrates, the peaks are not located at harmonics (or subharmonics) of a single primary frequency.

In contrast with single-mode and two-mode periodic solids, (i) the apparent contact angle exhibits a complex non-periodic waveform and (ii) the peaks of its power spectrum are no longer located at harmonics or subharmonics of a single primary frequency.

The contact line speed u_{cl_3} is plotted as a function of time in Figure 5.19. Similar to the periodic substrates, as the contact line recedes towards the centerline an overall decrease is observed in the local maxima of u_{cl_3} and the total evaporation is faster compared to the flat case (for the reference case presented, the average velocity of the contact line is approximately 5% larger than the constant contact line speed observed for the flat case). However, for this three-mode quasi-periodic substrate, the contact line exhibits a more complex and random behavior. Although the apparent stick-slip motion is observed in some regions the dynamics are much more complicated and hence it may not be interpreted as a pure step-like motion. It is to be expected that as the substrate becomes more complicated the spectrum will become broadened and the contact line speed will approximate a stationary random function.

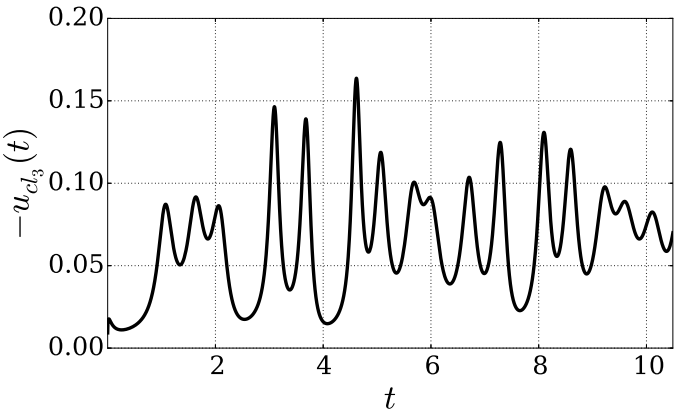

Figure 5.19: The contact line speed $u_{cl_3}(t)$ for the three-mode substrate produced by irrational wavelength ratios $\Omega_1 = 2\pi/3, \Omega_2 = \sqrt{\pi}$, and $\Omega_3 = 1$ and the specified contact angle $\theta_o = 5^o$. Neglecting the initial transient, the global average speed $\bar{u}_3$ for the data presented is equal to 0.068.

Chapter 6

SUMMARY AND CONCLUSION

In this work, evaporation of a symmetric liquid droplet is considered on both flat and curved substrate. The thermal control one-sided model is utilized to evaluate the evaporative mass flux along the liquid-vapor interface. An evolution equation for the drop thickness $h(x,t)$ is derived based on the lubrication approximation. Without requiring any pre-assumption for the shape of the drop, the problem is formulated based on a boundary condition of no capillary flow into the contact line and analyzed separately for the two evaporation modes: pinned contact line and moving contact line with constant contact angle. A numerical algorithm is developed using method of lines and finite difference schemes. The evolution equation and boundary conditions are discretized in space and then a stiff ode solver is used to integrate the problem in time. For the case in which the contact line moves, the singularity at the contact line is treated by the numerical slip model. For each evaporation mode two types of substrates are considered: flat and periodic.

For flat substrates, we solve the evolution equation for different values of dimensionless parameters, i.e. T_w, M, and $\theta(0)$. The results follow the equation (2.61), provided for the evaporative mass flux J, indicating that the evaporation process is faster for larger values of T_w and/or smaller values of M.

Our results for the case of pinned contact line reveal that away from the contact line, the droplet thickness $h(x,t)$ decreases linearly over time for the entire process. At first, the contact angle $\theta(t)$ decreases almost linearly for a range of time. With decreasing $h(x,t)$ and $\theta(t)$ the thermal resistance decreases and thus the evaporative mass flux increases. Accordingly the contact angle drops rapidly until it becomes zero at a critical time t_{cr}. This happens at a finite time and in advance of the total evaporation; hence, we conclude that the $\theta \to 0$ does

not correspond to dry out but that it may signal depinning. We believe that after t_{cr} the evaporation may change to the third mode, in which both contact angle and wetted radius vary. Moreover, for given values of T_w when time approaches t_{cr} the contact angle scaled by its initial value illustrates self-similarity in M and thus, $\theta(t)/\theta(0)$ can be described via an asymptotic scaling law. Our attempts to analytically describe the final approach to the singularity proved unsuccessful, so we left this for later work.

For the case of moving contact line, both the droplet thickness $h(x,t)$ and wetted radius $r(t)$ decrease over time in a fashion such that the droplet retains a nearly constant shape consistent with the static solution of constant curvature. Hence results of simpler models, which *assume* that droplet keeps its initial static shape, are validated. In addition, the contact line recedes in a nearly constant speed. This can indicate that although decreasing $h(x,t)$ increases the value of evaporative mass flux $J(x,t)$ over time but with decreasing $r(t)$ the total evaporative mass flow rate and the total area of the droplet change in a manner that the contact line moves with a nearly constant speed during the whole process.

For the case of periodic substrates, the parameters T_w, M, and θ_o are chosen to be fixed and the problem is solved for variety of periodic and quasi-periodic substrates. Our results show that the dynamics for the case of pinned contact line on periodic substrates is qualitatively similar to what occurs on the flat surface, except that the thermal resistance depends on the local thickness, leading to an oscillatory component to the flux, and also that as the slope ratio of the substrate increases it takes more time to reach to the critical time t_{cr}, i.e. the time at which the local contact angle goes to zero.

In contrast with what we found for the flat substrate, our results for the single-mode periodic profiles with moving contact line indicate that the droplet cross-section varies from the initial circular shape and that the wetted radius $r(t)$ is a nonlinear oscillatory function of time. We found that the overall evaporation is faster compared to the flat substrates and that as the contact line recedes towards the center line, it exhibits an "apparent stick-slip" behavior including two phases: a relatively long "apparent-pinning" stage, in which the contact line

moves slowly, followed by a shorter, high-speed region in which the speed of the contact line shows a spike. Moreover, the apparent contact angle $\alpha(t)$ is found to be periodic, meaning that the time t_λ that it takes for the contact line to move over one wavelength is constant. As the maximum speed of the contact line decreases, the duration of the high-speed regions increases in such way that t_λ remains constant over the entire process. Finally, as expected from a nonlinear system with periodic coefficients, we found that all the peaks in the power spectrum of $\alpha(t)$ are located at harmonics of a single primary frequency f_p.

For the two-mode periodic solid profiles, our results show the same apparent stick-slip behavior, that the apparent contact angle is still periodic, that all the peaks of the power spectrum of α are located at the harmonics and subharmonics of a single primary frequency f_{p_2}, and that the overall evaporation is faster compared to the flat case. However, compared with the single-mode solid, the apparent contact angle is a more complex waveform and more harmonics and subharmonics are observed in its power spectrum. Additionally, we found that the nonlinearity is strong enough such that the solution of the two-mode profile may not be achieved from the single-mode results. In other words, the problem behaves as a phase-locking system and thus combining the corresponding single-mode frequencies in sums and differences, fails to predict the primary frequency f_{p_2}.

Finally, for a multi-mode quasi-periodic profile which resembles a random configuration, we found that while the evaporation is still faster compared to the flat case the contact line behavior is very complex and not limited to an apparent stick-slip motion. We also found that the apparent contact angle is no longer periodic and that the peaks in the power spectrum of the apparent contact angle are associated with different primary frequencies, i.e. the peaks are no longer located at harmonics or subharmonics of a single primary frequency.

BIBLIOGRAPHY

[1] V. S. Ajaev and G. M. Homsy. Steady vapor bubbles in rectangular microchannels. *Journal of colloid and interface science*, 240(1):259–271, 2001.

[2] D. M. Anderson and S. H. Davis. The spreading of volatile liquid droplets on heated surfaces. *Physics of Fluids (1994-present)*, 7(2):248–265, 1995.

[3] J. P. Burelbach, S. G. Bankoff, and S. H. Davis. Nonlinear stability of evaporating/condensing liquid films. *Journal of Fluid Mechanics*, 195:463–494, 1988.

[4] A. M. Cazabat and G. Guéna. Evaporation of macroscopic sessile droplets. *Soft Matter*, 6(12):2591–2612, 2010.

[5] P. G. De Gennes. Wetting: statics and dynamics. *Reviews of modern physics*, 57(3):827, 1985.

[6] R. D. Deegan, O. Bakajin, T. F. Dupont, G. Huber, S. R. Nagel, and T. A. Witten. Contact line deposits in an evaporating drop. *Physical review E*, 62(1):756, 2000.

[7] V. Dussan et al. The moving contact line: the slip boundary condition. *Journal of Fluid mechanics*, 77(04):665–684, 1976.

[8] Elizabeth B. Dussan V. and S. H. Davis. On the motion of a fluid-fluid interface along a solid surface. *Journal of Fluid Mechanics*, 65(01):71–95, 1974.

[9] L. Espin and S. Kumar. Droplet spreading and absorption on rough, permeable substrates. *Journal of Fluid Mechanics*, 784:465–486, 2015.

[10] H. P. Greenspan. On the motion of a small viscous droplet that wets a surface. *Journal of Fluid Mechanics*, 84(01):125–143, 1978.

[11] P. J. Haley and M. J. Miksis. The effect of the contact line on droplet spreading. *Journal of Fluid Mechanics*, 223:57–81, 1991.

[12] L. Kondic and A. L. Bertozzi. Nonlinear dynamics and transient growth of driven contact lines. *Physics of Fluids (1994-present)*, 11(11):3560–3562, 1999.

[13] A. Mazouchi, C. M. Gramlich, and G. M. Homsy. Time-dependent free surface stokes flow with a moving contact line. i. flow over plane surfaces. *Physics of Fluids (1994-present)*, 16(5):1647–1659, 2004.

[14] G. McHale, S. Aqil, N. Shirtcliffe, M. Newton, and H. Y. Erbil. Analysis of droplet evaporation on a superhydrophobic surface. *Langmuir*, 21(24):11053–11060, 2005.

[15] J. A. Moriarty and L. W. Schwartz. Effective slip in numerical calculations of moving-contact-line problems. *Journal of engineering mathematics*, 26(1):81–86, 1992.

[16] D. T. Moyle, M. S. Chen, and G. M. Homsy. Nonlinear rivulet dynamics during unstable wetting flows. *International journal of multiphase flow*, 25(6):1243–1262, 1999.

[17] N. Murisic and L. Kondic. On evaporation of sessile drops with moving contact lines. *Journal of Fluid Mechanics*, 679:219–246, 2011.

[18] R. G. Picknett and R. Bexon. The evaporation of sessile or pendant drops in still air. *Journal of Colloid and Interface Science*, 61(2):336–350, 1977.

[19] N. Savva and S. Kalliadasis. Two-dimensional droplet spreading over topographical substrates. *Physics of Fluids (1994-present)*, 21(9):092102, 2009.

[20] N. Savva and S. Kalliadasis. Droplet motion on inclined heterogeneous substrates. *Journal of Fluid Mechanics*, 725:462–491, 2013.

[21] N. Savva, S. Kalliadasis, and G. A. Pavliotis. Two-dimensional droplet spreading over random topographical substrates. *Physical review letters*, 104(8):084501, 2010.

[22] Martin E. R. Shanahan. Simple theory of "stick-slip" wetting hysteresis. *Langmuir*, 11(3):1041–1043, 1995.

[23] J. M. Stauber, S. K. Wilson, B. R. Duffy, and K. Sefiane. On the lifetimes of evaporating droplets. *Journal of Fluid Mechanics*, 744:R2, 2014.

[24] J. M. Stauber, S. K. Wilson, B. R. Duffy, and K. Sefiane. On the lifetimes of evaporating droplets with related initial and receding contact angles. *Physics of Fluids (1994-present)*, 27(12):122101, 2015.